PHYSICAL REVIEW D VOLUME 9, NUMBER 7 1 APRIL 1974

Large-angle proton and pion production in deep-inelastic electron scattering*

L. Ahrens, K. Berkelman, G. S. Brown,† D. G. Cassel,‡ W. R. Francis,§ P. H. Garbincius, D. Harding, D. L. Hartill, J. L. Hartmann, R. L. Loveless,|| R. C. Rohlfs,¶ and D. H. White
Laboratory of Nuclear Studies, Cornell University, Ithaca, New York 14850

A. J. Sadoff
Physics Department, Ithaca College, Ithaca, New York 14850

(Received 30 November 1973)

We have measured ep, $e\pi^+$, and $e\pi^-$ coincidences for scattered electrons in the range $Q^2=0.4$ to 2.2 GeV^2 and $W=2$ to 4 GeV. We find (a) that vector-meson production decreases with Q^2 more rapidly than does the total virtual-photon–plus–proton cross section, more rapidly even than the prediction of simple vector dominance, (b) that the slope of the t distribution in ρ and ω production becomes flatter with increasing Q^2 and seems to be at least approximately a function of the single variable $x_\rho = (Q^2 + m_\rho^2)/2M\nu$, (c) that the fraction of final states containing a proton decreases with increasing Q^2, (d) that in the central region of longitudinal momenta the inclusive π^+ yield seems to increase relative to the π^- yield as Q^2 increases, and (e) that the average transverse momentum of π^- is greater than of π^+ in the central region of longitudinal momenta.

I. INTRODUCTION

The first inelastic electron scattering experiments[1] to explore the region of final-state hadron effective mass[2] W beyond the nucleon resonances revealed a cross section which decreases less rapidly with increasing four-momentum transfer squared Q^2 than does the elastic cross section. The nucleon structure function[1] $\nu W_2(Q^2, W)$ was found to obey scaling[3] for $Q^2 > 1\,\text{GeV}^2$. These observations inspired the parton model,[4] in which the inelastic scattering is the incoherent sum of elastic scatters from pointlike constituents in the nucleon. It is also possible, however, to understand the data using the vector-dominance approach,[5] in which the scattering comes about through the interaction of the hadronic constituents of the virtual photon with the target nucleon.

In an effort to choose among these and other models, to reveal the nature of the partons, if they exist, or to see the diffractively produced hadronic components of the photon, experimenters have recently been observing the hadronic final states in inelastic electron (or muon) scattering.[6,7] In one class of experiments the collision occurs inside a hydrogen bubble chamber[8] or streamer chamber[9] and all charged products are observed. To overcome the limited statistics and the difficulty of particle identification inherent in this technique, other experimenters have concentrated on observing one or a few hadrons in a limited angular range using typically a high-resolution spectrometer with particle identification in coincidence with another spectrometer for electrons. In this latter class there are experiments designed to detect forward-produced hadrons,[10-14] and others,[15-17] such as the work we are reporting here, sensitive to particles produced backward in the center-of-mass frame.

Our experiment is a sequel to similar experiments performed earlier at Cornell with different apparatus and reported elsewhere.[18-21] The present experiment covers a much wider range in Q^2 and W and is based on an order of magnitude more events. A preliminary report of some aspects of the experiment has already been published.[22] Figure 1 shows the layout of the apparatus. Electrons scattered through about 8° in the hydrogen target were detected in one spectrometer in coincidence with protons or pions produced between about 40° and 80° and detected in another spectrometer.

II. BEAM AND TARGET

The incident electron beam was extracted from the Cornell 12-GeV electron synchrotron using the usual resonance method, brought to the experimental area through a conventional beam transport system of quadrupole and bending magnets, and focused on the experimental target. At the target the beam spot was typically 2 mm vertically by 4 mm horizontally, with an angular divergence about 0.3 mrad. The beam pulse rate was 60 per second, each pulse lasting for about 1.6 msec. During the beam pulse the intensity had a 2.5-μsec time structure, corresponding to the circulation period in the synchrotron ring, which resulted in a typical duty cycle of about 50% during the beam pulse. The over-all beam duty cycle was therefore about 4%.

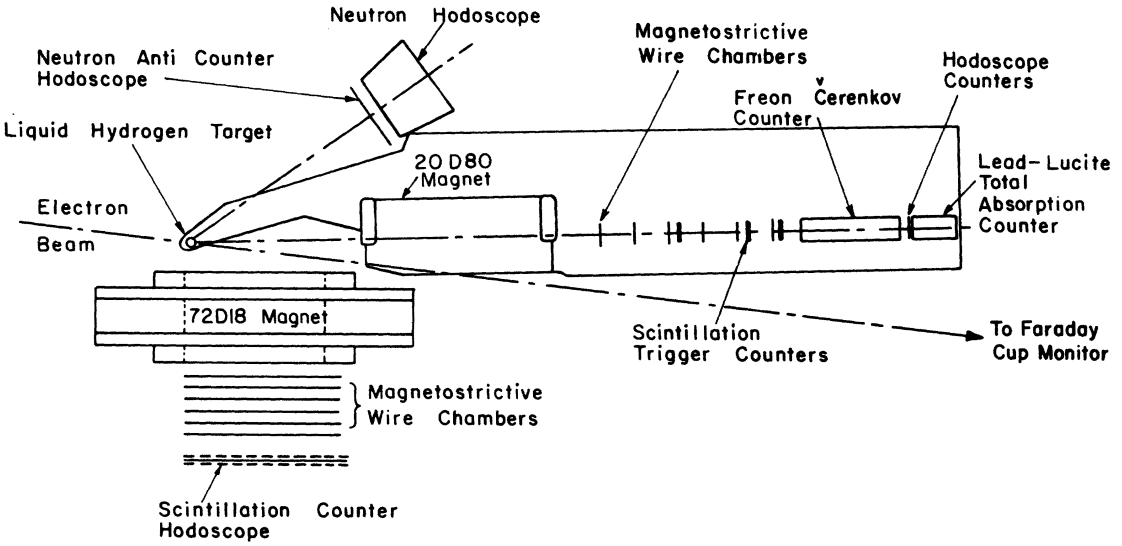

FIG. 1. Layout of the experiment. The neutron hodoscope was used in another experiment (Ref. 31), run parasitically with the one reported here.

During the course of the experiment, data runs were taken with 8.0-, 10.0-, and 11.8-GeV synchrotron energies. Because the instantaneous beam energy varied sinusoidally, there was a spread in energies of about 2% during the extraction time. This did not affect the accuracy of the data, since the instantaneous beam energy was recorded with the data for each event observed. This beam energy measurement has been calibrated by magnetic deflection[23] to an accuracy of 0.3%.

In order to limit the probability of accidental coincidences, the time-averaged beam intensity was set at about 3×10^{10} electrons per second. The total number of electrons passing through the target was monitored by measuring the charge collected in a Faraday cup 12 m downstream of the target. The Faraday cup had been intercalibrated with another Faraday cup, a mercury calorimeter, and a secondary-emission quantameter.[24] All agreed within 1%.

The positioning of the beam at the Faraday cup was monitored continuously by a phosphor screen viewed remotely by a television camera. The beam position at the target was checked several times a day by inserting another remotely viewed phosphor screen into the beam immediately downstream of the target.

The target was a 0.5-in vertical cylinder of 0.001-in. kapton film filled with liquid hydrogen.

III. ELECTRON SPECTROMETER

Scattered electrons passed through the 5-in. gap of a 20*D*80 bending magnet[25] (see Fig. 2) and were deflected upward through an angle of 10° to 15°. They then passed through six wire spark chambers and three scintillators, then through a threshold gas Čerenkov counter, an array of five hodoscope scintillators, and a total absorption lead-lucite shower telescope. All spectrometer components were mounted on a platform pivoted at the hydrogen target.

The spark chambers each had an interior area of 10×40 square inches. Each chamber had one plane with vertical wires and one with wires slanted 10° from the horizontal. The slant of the wires in the third and fourth chambers was opposite to that in the remaining four chambers to permit resolution of multiple tracks.

The three scintillators, situated as shown in Fig. 2, each had a 10×40-square-inch active area; the third one defined the angular aperture of the spectrometer. The gas Čerenkov counter was filled with Freon-12 gas at 3 atm. The counter was sensitive to electrons and to pions of momentum greater than about 2 GeV/c. The vertical aperture was subdivided into five intervals by the hodoscope array. The hodoscope information was used to select the correct track when several tracks were seen in the chambers. The shower detector consisted of eight sheets of $20\times60\times1$-in. Lucite interleaved with 0.25-in. sheets of lead. Each Lucite sheet was viewed with a photomultiplier; the outputs were added.

An electron trigger consisted of a fast coincidence of the three scintillation counters and the shower telescope. The scintillator thresholds were set to count minimum-ionizing particles with 99% efficiency, and the shower-counter

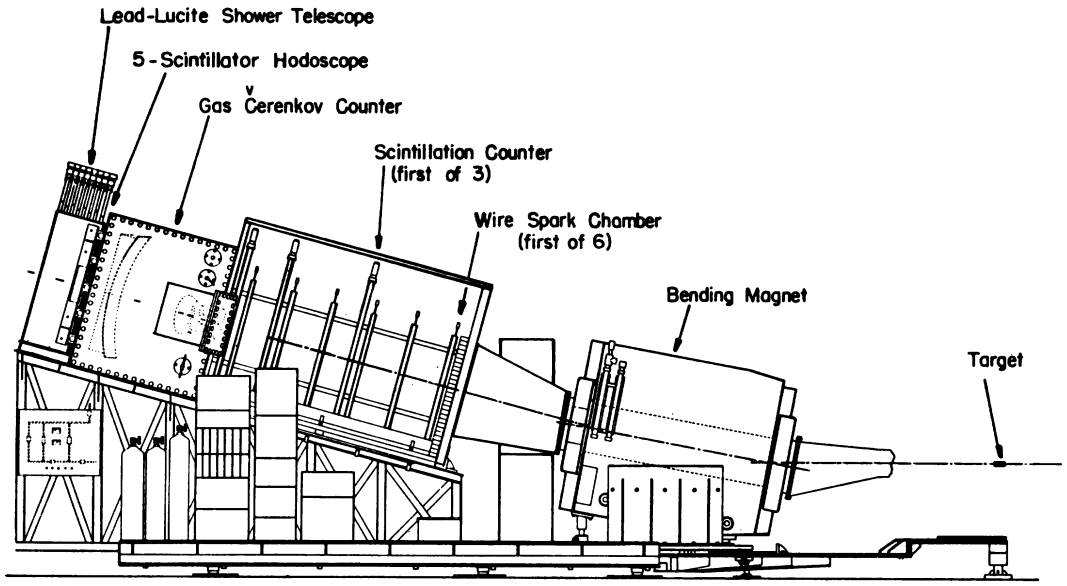

FIG. 2. Side view of the electron spectrometer.

threshold was set below the average pulse height for 2-GeV electrons. Although the hodoscope and gas Čerenkov counter were not included in the trigger, their pulse information was recorded with each event.

We calculated[26] the trajectory of a particle behind the bending magnet from the spark-chamber information. A track in either the x or y projection had to contain at least four sparks in a straight line. The track-finding efficiency, computed from the relative numbers of 4-, 5-, and 6-spark tracks, was 99.9%.

We rejected a track if its extrapolation did not pass through the defining scintillator or the magnet gap. Otherwise it was projected back through the magnet gap to the target. Assuming a uniform field in the magnet gap, we fitted to a helical trajectory in the magnet and iterated until the radius of curvature (and hence the momentum) was found which resulted in zero vertical displacement at the target position (assumed to be a point).

To decide if the detected particle was an electron, we examined the gas Čerenkov and shower pulse heights. Electrons counted in the gas counter and made large pulses, proportional to momentum, in the shower counter. To improve the resolution we corrected the shower-counter pulse height for the dependence on the distance between the particle track and the photomultipliers and for the attenuating effect of several reinforcing bars in the gas counter. Pions were sometimes counted in the Čerenkov counter, depending on their velocity, and generally had small pulses in the shower detector. Most of the pions could be rejected by requiring a count in the Čerenkov counter and a minimum value of shower pulse height divided by momentum. Since the electronic threshold in the shower counter was set conservatively low, some 20–40% of the triggers were rejected as pions. Since the tail of the pion-shower pulse-height distribution extended under the electron peak [Fig. 3(a)], we had to make a subtraction of this contamination. The number of events to be subtracted was deduced from the shape of the tail of the pion-shower spectrum, as seen in the events which did not have Čerenkov pulses

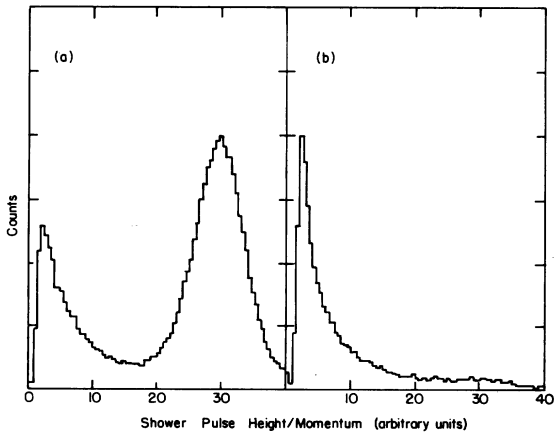

FIG. 3. (a) Sample spectrum of electron shower pulse height divided by particle momentum for events which were detected in the gas Čerenkov counter. The pulse heights have been corrected as described in the text. (b) Same for events which did not count in the gas counter.

[Fig. 3(b)].

The root-mean-square momentum resolution was observed to be 0.5% from the shape of the elastic electron scattering peak. This value is compatible with the known effects of multiple scattering in the spectrometer, spatial resolution in the spark chambers, magnetic field inhomogeneity, and finite target size.

The momentum and angle acceptance[26] of the spectrometer is determined by the aperture and field of the bending magnet and by the third scintillation counter. The spectrometer accepts 25.6 mrad horizontally, essentially independent of momentum; the vertical angle limits depend on momentum and are shown in Fig. 4 as a function of the reciprocal particle momentum relative to the "nominal" central momentum determined by the magnet current. Figure 5 shows the acceptance solid angle as a function of momentum divided by nominal momentum. For any fixed setting of the magnet current the accepted momentum range is approximately $p_{\text{nominal}} \times (1^{+\infty}_{-0.5})$, or $p_{\text{nominal}} \times (1^{+1.0}_{-0.3})$ at half maximum aperture. This property of the spectrometer makes it possible to cover in one magnet current setting essentially the complete spectrum of scattered electron energy E' at fixed incident energy E and scattering angle θ_e.

Data were taken at fixed spectrometer angle of 8.21°, at three different incident beam energies: 8, 10, and 11.8 GeV. The magnet current was set to correspond to $p_{\text{nominal}} = 3.89$, 4.95, and 4.95 GeV/$c$ in the three runs. The kinematic region in Q^2 and W covered by the acceptance of the electron spectrometer is shown in Fig. 6. In order to study the Q^2 and W dependence, we divided the data for each incident energy E into five bins. Bin boundaries where chosen to correspond to lines of constant $\omega' = 1 + W^2/Q^2$, actually at $\ln \omega' = 1.0$, 1.5, ..., 3.5. Relevant parameters for each bin are given in Table I.

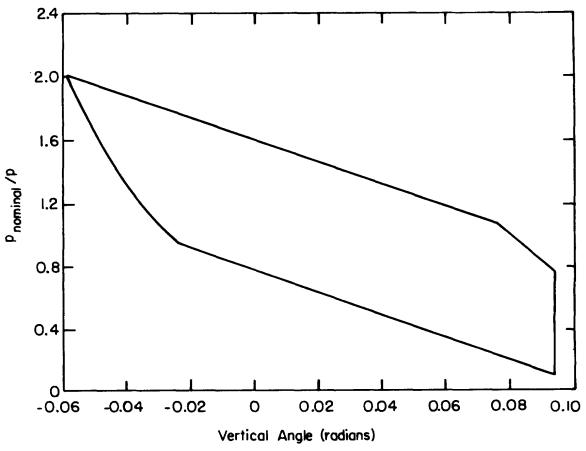

FIG. 4. Electron spectrometer geometrical acceptance boundaries in p_{nominal}/p vs tangent of vertical angle. The values of p_{nominal} in the various data runs are listed in Table II.

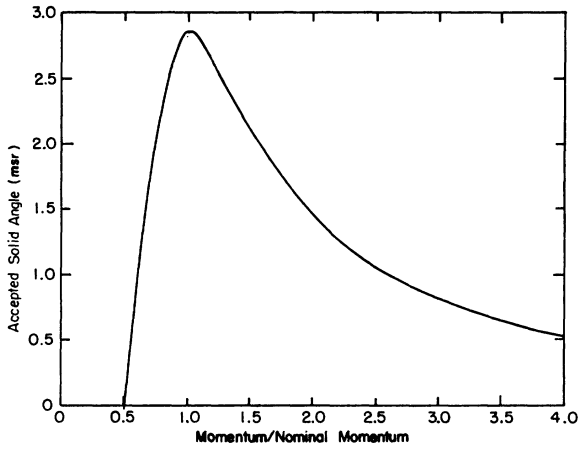

FIG. 5. Acceptance solid angle as a function of p/p_{nominal} for the electron spectrometer. For p_{nominal} values, see Table II.

IV. HADRON SPECTROMETER

The hadron spectrometer[27] consisted of a 72D18 magnet with a 24-in. gap height, bending in the horizontal plane, followed by six wire spark chambers and two planes of scintillation counters (see Fig. 7). The magnet was positioned with its 72-in. length converging toward the downstream beam line at a 6.1° angle, and its gap centered vertically on the beam height. The volume from the target vacuum chamber window to the first spark

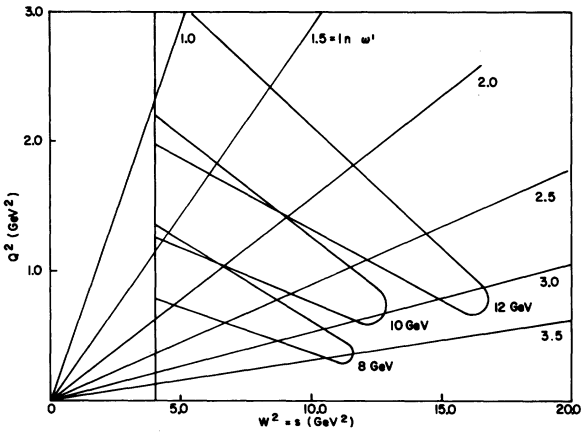

FIG. 6. The acceptance regions for the three data runs, in the Q^2 vs W^2 plane. The curved lines outline the geometric acceptance; the straight lines radiating from the origin are the lines of constant ω' along which the data were divided. No data below $W = 2$ GeV were used in the analysis.

TABLE I. Average kinematics for each of the five ω' bins at each of the three incident energies E. The average is weighted by the virtual-photon flux Γ and the experimental acceptance.

E (GeV)	$\ln\omega'$	ω'	Q^2 (GeV^2)	W (GeV)	ν (GeV)	ϵ
8.0	1.0–1.5	4	1.26	2.10	2.4	0.93
	1.5–2.0	6	0.99	2.17	2.7	0.92
	2.0–2.5	10	0.78	2.57	3.5	0.85
	2.5–3.0	15	0.59	2.92	4.4	0.74
	3.0–3.5	25	0.43	3.20	5.2	0.62
10.0	1.0–1.5	4	1.61	2.19	2.9	0.93
	1.5–2.0	6	1.37	2.57	3.8	0.89
	2.0–2.5	10	1.06	3.01	4.9	0.80
	2.5–3.0	15	0.80	3.38	6.0	0.68
	3.0–3.5	25	0.61	3.62	6.8	0.57
11.8	1.0–1.5	4	2.23	2.39	3.8	0.92
	1.5–2.0	6	1.78	2.93	5.1	0.85
	2.0–2.5	10	1.36	3.39	6.4	0.75
	2.5–3.0	15	0.99	3.77	7.6	0.62
	3.0–3.5	25	0.74	4.01	8.6	0.51

chamber was filled with helium gas. The region of the magnet gap forward of a line through the target making a 30° angle to the beam line was filled with lead to shield the wire chambers and counters from scattering sources downstream of the target. The magnetic field was fixed throughout the course of the experiment, and produced a nominal

$$p\theta = (30\ \text{MeV/kG m}) \int Bdl$$

equal to 130 MeV/c.

Each of the wire spark chambers had one plane with vertical wires. The first, third, and fifth chambers also had one plane of horizontal wires; in each of the remaining three chambers the second plane of wires was oriented at 15° from the vertical. The active area of each chamber was 80×40 square inches.

Two planes of 0.375-in.-thick scintillation counters separated by 0.25 in. of aluminum were used to detect the passage of charged particles through the spectrometer.[26] Each plane consisted of eleven counters, 7.375 in. wide by 40 in. tall. Each counter was viewed by a photomultiplier at each end; the output signals from each pair were added.

The hadron trigger requirement was (a) a fast coincidence between corresponding scintillators in the front and rear banks, with thresholds set

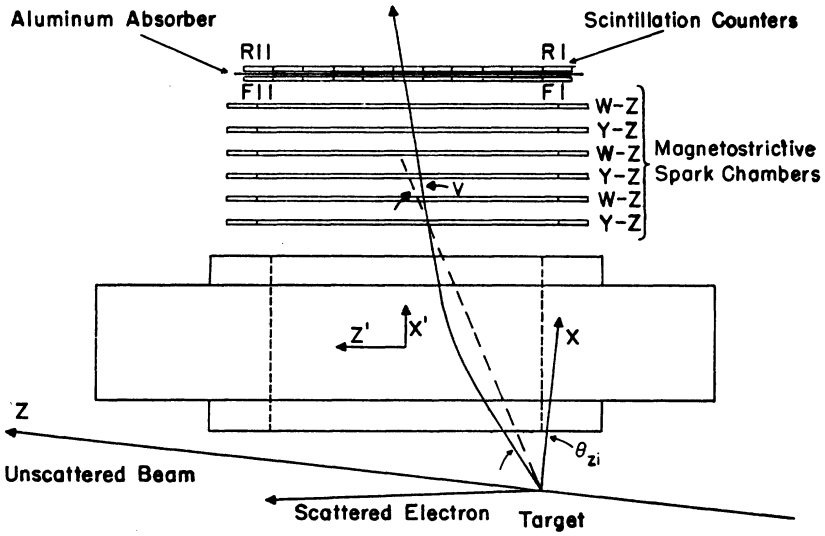

FIG. 7. Plan view of the hadron spectrometer.

below the level appropriate for minimum-ionizing particles, or (b) a single pulse in the front bank with a threshold set at a level three times higher. Figure 8 shows the expected amount of energy deposited in the front and rear counters as a function of the momentum (at the target) for a proton. The curves demonstrate that we were sensitive to all protons of momentum greater than 240 MeV/c. The corresponding threshold for pions was actually below the minimum momentum which could pass through the magnetic field.

We required a hadron track to be a straight line containing sparks from at least four of the six planes of vertical wires and from at least two each of the three planes of horizontal wires and of diagonal wires. In addition, the extension of each track had to pass within one inch of a triggered hadron scintillator. We have studied the spark-chamber spatial resolution by examining the straightness of tracks for particles with momenta above 800 MeV/c. The full width at half maximum of the peak in the spectrum of miss distances between spark and best straight line was about 0.1 in. After the experiment was completed this was traced to a wiring error in the spark digitizing scalers, which introduced a 0.080-in. random error in the computed position of the spark. Although the error could have been eliminated by reprocessing all of the data, we did not consider the effort worthwhile, since multiple scattering dominated the spatial resolution at low momentum, where most of the data were.

We reconstructed hadron momenta using look-up tables which mapped the track coordinates in the wire chambers into hadron momentum components at the target. The tables were generated[27] by numerically integrating a representative family of trajectories from the target to the first wire-chamber plane through the rather nonuniform field of the magnet.[28] In order to account for the effects of ionization energy loss along the track, we generated separate tables for protons and pions. The tables connected values of p_x, p_y, p_z at the target with the horizontal and vertical coordinates of the trajectory at the first spark-chamber plane, and with V, the difference in tangents between the horizontal projection of the track in the chambers and the straight line connecting that point with the target (see Fig. 7). V was roughly a measure of reciprocal momentum. The 0.5-in.-long target was treated as a point and used as a constraint on each trajectory, since the track was not measured between target and magnet. The tables also contained the calculated time of flight from target to counter bank for each trajectory and the vertical slope at the first chamber plane.

Each hadron event was reconstructed by interpolating in V and the horizontal and vertical position to get p_x, p_y, p_z from the table. For each event we compared the tabulated and observed values of the vertical slope of the track (not used in the reconstruction), and required that they

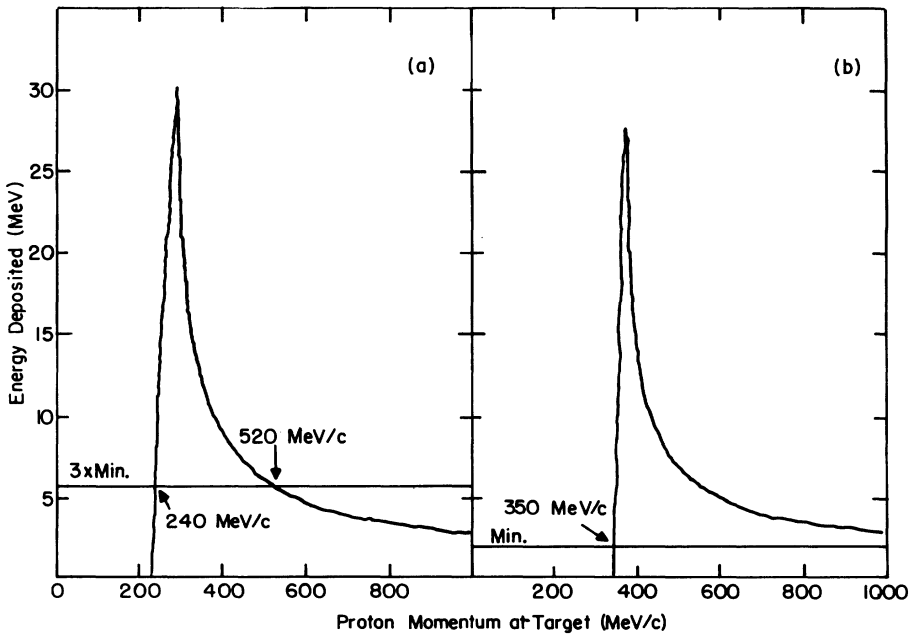

FIG. 8. (a) The calculated mean energy deposited in the front counters as a function of proton momentum at the target. (b) The same for the rear counters.

agree within 35 mrad (20.5 mrad for pions) in order to eliminate accidental tracks, pion decays, secondaries from interactions in the magnet poles, and so on.

The reconstruction of each event was done twice, using both proton and pion look-up tables. The observed time delay between the electron and hadron triggers was corrected for pulse-height slewing, light propagation time in the scintillators and light pipes, and cable delay differences among the hadron counters and then compared with the predicted flight times from the proton and pion tables. If the observed time was within 1.5 nsec of the tabulated pion time, we accepted the hadron as a pion. Figure 9 shows typical timing spectra at two momenta. The protons, because of multiple scattering, had broader timing spectra (Fig. 10). At low momenta the proton timing limits were made wider (up to 4.3 nsec at 275 MeV/c) to accommodate the increased spread. Hadrons with measured momenta above 1 GeV/c were not used in the analysis, since the identification by time of flight became ambiguous for fast particles.

Events which failed the proton and pion timing cuts were either accidental coincidences, decay or interaction products, or K mesons. A significant kaon timing peak was observed, but it was not possible to extract a quantitatively reliable cross section because of the accidental background.[29] Table II gives a summary tally of the numbers of events falling in the various categories.

The reconstruction look-up tables also provided information on the geometrical acceptance boundaries. Figure 11 shows the vertical acceptance (maximum tangent of vertical angle at the target) as a function of reciprocal momentum and horizontal angle relative to the beam. The figure is plotted for π^+ mesons; the acceptance for protons is rather similar, except for the effects of increased ionization loss at low momenta.

V. DATA CORRECTIONS

For the major portion of the data taken at the three incident energies, the field polarity in the hadron magnet was such as to deflect positive particles to larger angles, thus maximizing the aperture for positive hadrons. In this condition there was a somewhat smaller aperture, centered on larger production angles, for negative hadrons. In order to compare π^+ and π^- production in the same angular ranges, we took a smaller amount of data with the magnetic field reversed in the hadron magnet.

Data were also taken with the target empty to determine the fraction of the normal data rate coming from production in the kapton target walls. These data were supplemented by data from a much thicker carbon target to determine more accurately the momentum distributions of protons and pions produced in the target walls. We found

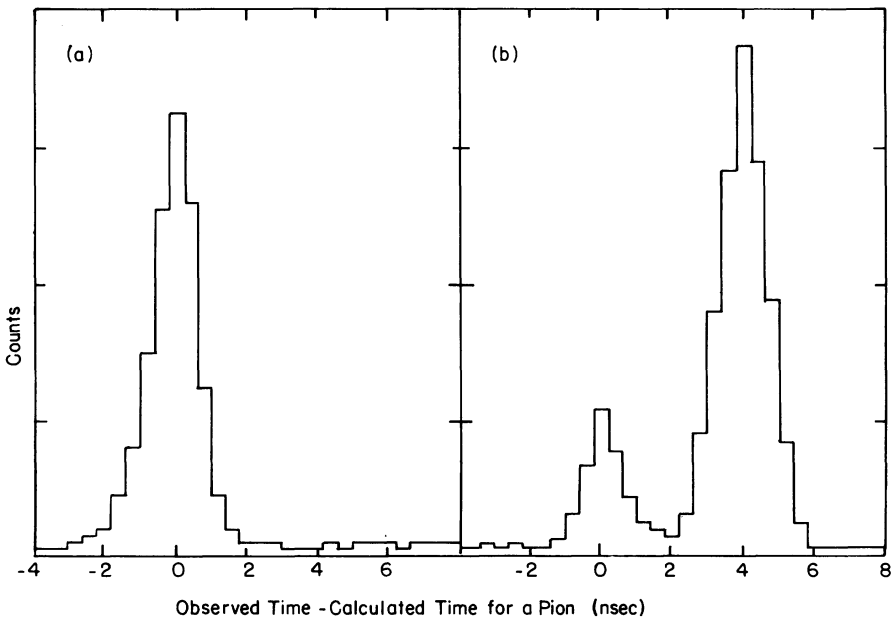

FIG. 9. (a) Time-of-flight spectrum: number of events vs observed flight time minus calculated flight time, assuming pion kinematics, for momenta between 0.2 and 0.3 GeV/c. (b) Same for momenta between 0.9 and 1.0 GeV/c. The peaks at zero correspond to pions.

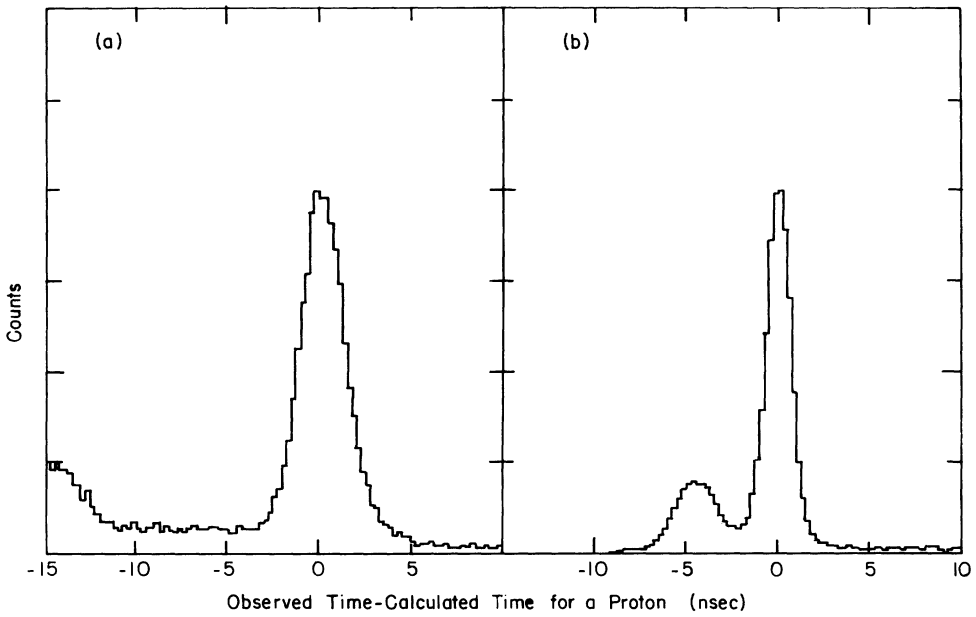

FIG. 10. (a) Time-of-flight spectrum: number of events vs observed flight time minus calculated flight time, assuming proton kinematics, for momenta between 0.32 and 0.39 GeV/c. (b) The same for momenta between 0.95 and 1.13 GeV/c.

that these distributions showed no structure, but instead followed closely the distributions expected from just the geometric acceptance.

We discovered in the analysis of the data that there had been a slow leak in the target vacuum chamber, resulting in condensation on the liquid hydrogen target. The effect of this frost was determined for each data run from the rise in scattered electron counting rate, which increased linearly with time from the last target warmup. The frost background was subtracted from the data in the same way as the target wall background. The subtraction varied from 0 to 50%.

Other subtractions in the data were made to account for spurious events which survived the various data cuts. Background pions which escaped the pulse-height cut in the electron shower counter were subtracted using a sample of pion events below the pulse-height threshold. We subtracted the flat background of events under the peak in the vertical slope distribution by using events outside the peak region suitably normalized. A similar procedure was used for the random and decay backgrounds under the proton and pion time-of-flight peaks. Such subtractions amounted to about 15% of the data.

Since the flux of particles through the hadron spectrometer was quite high, the detection efficiency was somewhat lower than for ideal single tracks. We measured the track efficiency in the actual data by making use of the fact that a large fraction of the radiative scattering events ($e+p \rightarrow e+p+\gamma$) were identifiable without making use of the hadron spark-chamber information.

TABLE II. Efficiencies and event numbers for the three data runs.

E = incident electron energy (GeV)	8.0	10.0	11.8
p_{nominal} (GeV/c)	3.9	5.0	5.0
Electron detection efficiency	0.98	0.95	0.96
Hadron detection efficiency	0.95	0.86	0.78
Number of incident electrons	2.1×10^{16}	3.8×10^{16}	2.4×10^{16}
Triggers	1.1×10^{6}	1.1×10^{6}	0.7×10^{6}
Reconstructed events	730×10^{3}	690×10^{3}	430×10^{3}
ep events	150×10^{3}	220×10^{3}	120×10^{3}
Radiative ep events (forward peak)	58×10^{3}	55×10^{3}	23×10^{3}
Vector-meson ep events	4.3×10^{3}	3.5×10^{3}	1.5×10^{3}
$e\pi^{+}$ events	59×10^{3}	72×10^{3}	32×10^{3}

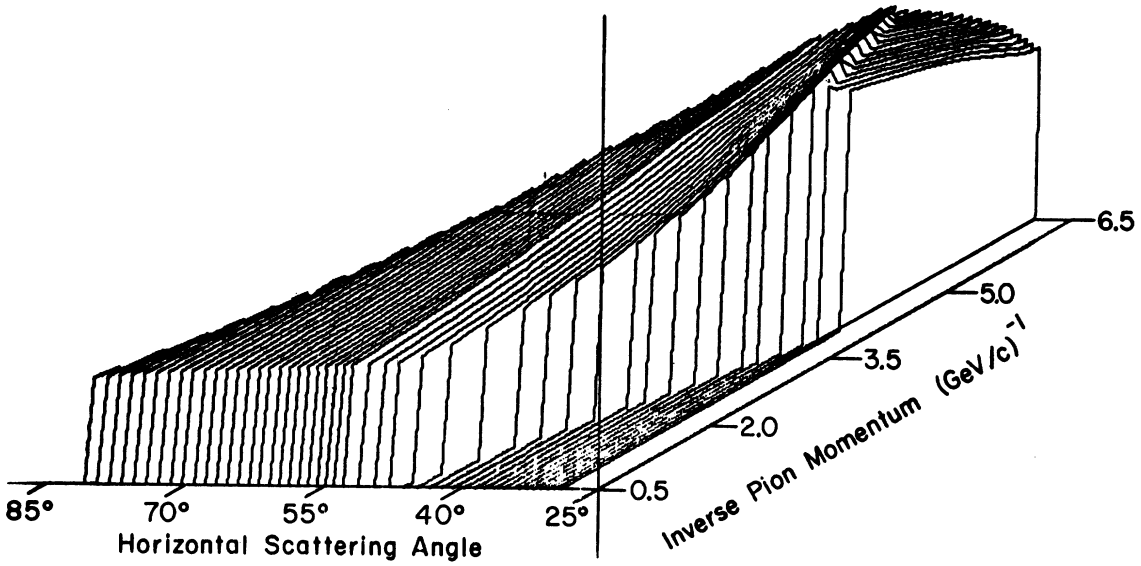

FIG. 11. Vertical aperture (tangent of maximum vertical angle) for pions in the hadron spectrometer as a function of horizontal angle relative to beam and reciprocal momentum.

Comparing the fractional contribution of these radiative events with (a) the number of triggers with an acceptable track and with (b) the number of triggers without tracks, we could tell how many no-track triggers should have had tracks and how many triggers were spurious, and hence derive the track efficiency. We verified the trigger-counter efficiency by examination of the pulse-height spectra. Corrections were applied to the data in the case of two trigger scintillators whose gains were not sufficient to count fast pions with full efficiency. Average efficiencies for the hadron and electron spectrometers are listed in Table II.

VI. PROTON EXCLUSIVE RESULTS

For each electron-proton coincidence event we computed m_x^2 the square of the missing mass in the reaction $e+p\rightarrow+p+x$, and t the square of the four-momentum transfer from target proton to final proton. For an initial proton at rest t depends only on the laboratory energy of the outgoing proton: $t=-2M(E_p-M)$. The missing mass depends mainly on the proton lab angle, but also somewhat on the proton energy. The ep coincidence data in each of the fifteen E, ω' bins (see Fig. 6 and Table I) were further subdivided into bins of width 0.05 GeV^2 in m_x^2 and of width 0.1 GeV^2 in t. The appropriate background subtractions (see above) were made separately for each E, ω', m_x^2, t data set.

To obtain for each bin the average cross section $d\sigma/dm_x^2dt$ for the virtual-photon reaction $\gamma_v+p\rightarrow p+x$ we divide the corrected number of events by the number of incident electrons, the target density, the bin widths $\Delta m_x^2\Delta t$, the virtual-photon flux factor[30]

$$\Gamma=\frac{\alpha}{2\pi^2}\frac{E'}{E}\frac{W^2-M^2}{2MQ^2}\frac{1}{1-\epsilon}, \tag{1}$$

where

$$\epsilon=[1+2(1+\nu^2/Q^2)\tan^2(\theta_e/2)]^{-1}, \tag{2}$$

and the geometric probability of detection. The latter two factors are evaluated by a Monte Carlo integration over the acceptance ranges in $\vec{p}_e'$ and $\vec{p}_p$ for the two spectrometers.

In principle, the cross section for $e+p\rightarrow e+p+x$ can depend on six independent kinematic variables (provided polarizations are not observed): for example, E, E', and θ_e for the electron and p_p, θ_p, and ϕ_{pe} for the proton; or alternatively, Q^2, W, ϵ, m_x^2, t, and ϕ(the proton azimuth about the virtual-photon axis). Since the θ_e aperture of the electron spectrometer was only 25.6 mrad wide and the spectrometer angle was fixed throughout the experiment, we are not able to study the dependence of the cross section on θ_e. This means that as we change Q^2 and W in going from one data set to another, we also vary the photon polarization ϵ (see Table I). Although in the interpretation of the data we treat the variations in cross section as trends in Q^2 and W, it is possible, especially if there are strong contributions from longitudinal photons, that we are seeing ϵ dependence as well.

Also, because of the limited aperture (about $\pm 30°$) in proton-electron azimuthal angle ϕ_{pe}, we are not able to study the dependence of the virtual-photon

cross sections on ϕ. The aperture calculation is averaged over ϕ, and the quoted cross sections $d\sigma/dm_x{}^2dt$ represent integrals over ϕ, deduced from the data for $d\sigma/dm_x{}^2dt\ d\phi$ at $\phi \approx \pi$ by assuming no azimuthal dependence. Other experiments[9,14,31,32] have established that the ϕ dependence in electroproduction cross sections for $W > 2$ GeV is weak or absent. A $\cos 2\phi$ term would arise from interference between the two transverse photon polarization amplitudes and a $\cos\phi$ term would indicate transverse-longitudinal interference. To avoid the nucleon resonance region and possible ϕ variations, we have included only data with $W > 2$ GeV in the analysis.

Figure 12 shows sample plots of $d\sigma/dm_x{}^2dt$ as a function of $m_x{}^2$ for various E, ω', t. The experimental resolution in $m_x{}^2$ varied from typically 0.03 GeV^2 (rms) at low t to 0.1 GeV^2 at high t, and was predominantly determined by the momentum and angle resolution of the hadron spectrometer. The geometrical acceptance was generally uniform in $m_x{}^2$ for $-t > 0.075$ GeV^2 and up to a limit in $m_x{}^2$ which exceeded 0.8 GeV^2 and increased with increasing W.

For each bin in E, ω', and t we fitted the $m_x{}^2$ spectrum with a sum of four contributions: (1) a Gaussian peak at $m_x{}^2 = 0$ with width consistent with experimental resolution, corresponding mainly to radiative ep scattering; (2) a peak at $m_x{}^2 \approx 0.6$ GeV^2 from ρ^0 and ω electroproduction; (3) a ϕ

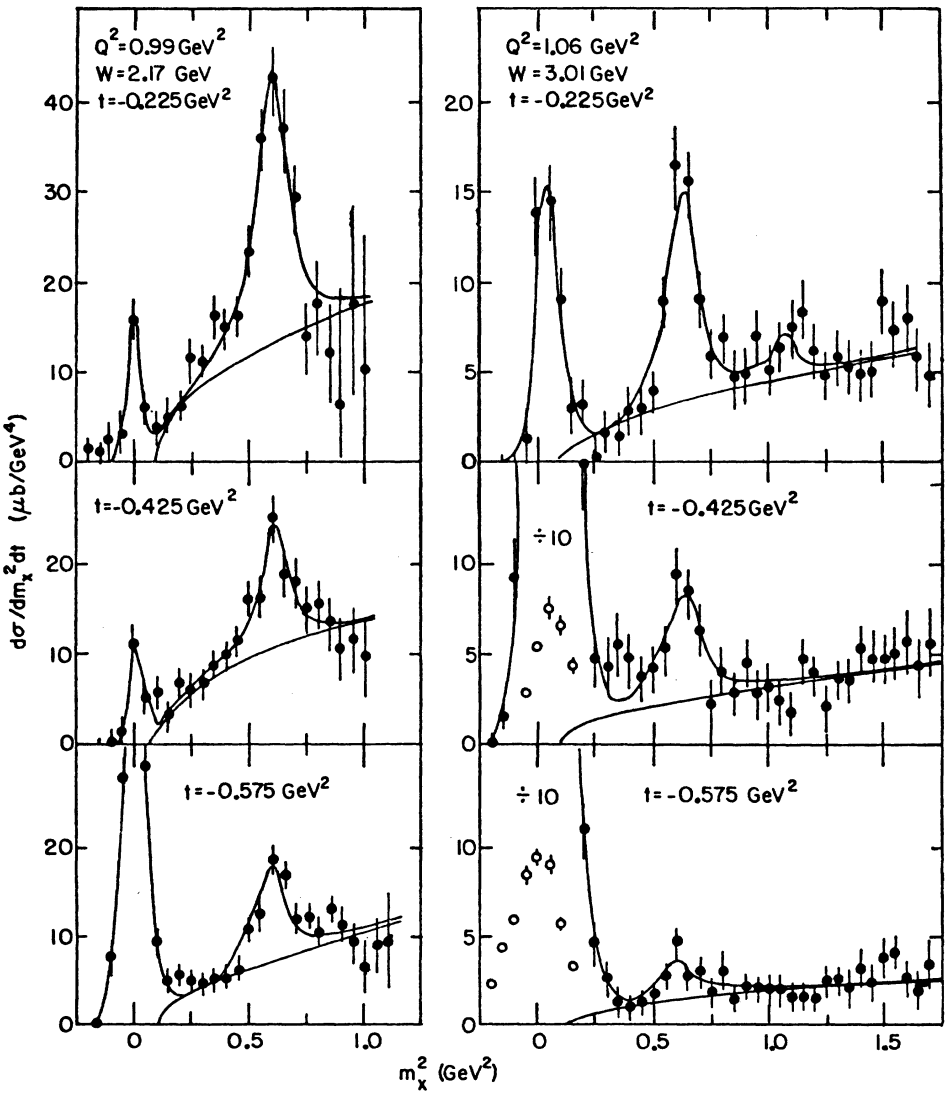

FIG. 12. Sample missing-mass-squared spectra for $\gamma_v + p \to p + x$. The curves show the results of the fit described in the text.

peak at $m_x^2 \approx 1.04$ GeV^2; and (4) a continuum starting at $m_x^2 = 4m_\pi^2$.

The missing momentum for events in the zero-mass peak shows a strong peaking in the incident beam direction (Fig. 13) and a weaker peaking in the scattered electron direction, as one would expect for bremsstrahlung events. Agreement with the expected rate,[27] obtained by integrating the theoretical differential cross section[33] over the experimental apertures, is typically only within 20%. The discrepancy is not significant, since a large portion of the radiative events occurs with the proton going very near the edge of the aperture where the acceptance is rapidly varying and not well enough known for a sharp peak. Furthermore, π^0 events at $m_x^2 = m_\pi^2 = 0.02$ GeV^2 are indistinguishable from radiative events because of the finite resolution. The mass fitting also includes the effect of an estimated two-photon tail on the zero-mass peak.

The experimental resolution in m_x^2 also prevents a reliable separation of ρ^0 and ω contributions. The shape of the $\rho\omega$ peak used in the fitting is fixed by starting with a relativistic Breit-Wigner form with a p-wave width,[34] multiplied by a generalized Ross-Stodolsky factor,[35] then adding on a Breit-Wigner ω peak with an area fixed at 15% of the ρ peak.[36] That is,

$$\frac{d\sigma}{dm_x^2 dt} = \frac{d\sigma_{\rho\omega}}{dt}\left[\frac{1}{1.15}\,\frac{m_\rho^2\Gamma_\rho^2}{(m_x^2-m_\rho^2)^2+m_\rho^2\Gamma_\rho^2} \times\left(\frac{m_\rho^2+Q^2-t}{m_x^2+Q^2-t}\right)^2 + \frac{0.15}{1.15}F_{\mathrm{BW}}(m_x^2-m_\omega^2)\right], \tag{3}$$

where

$$\Gamma_\rho = \frac{m_\rho}{m_x}\left(\frac{m_x^2-4m_\pi^2}{m_\rho^2-4m_\pi^2}\right)^{3/2}\Gamma_0. \tag{4}$$

The radiative correction, calculated for each E, ω', and t from a modified version of the formula given by Bartl and Urban,[37] is then applied to this shape function, resulting in a lowering of the peak height and the addition of a tail extending to higher masses. Finally, the resulting shape function is convoluted with the experimental resolution function to yield the $\rho\omega$ peak shape used in the least-squares fit to the m_x^2 spectrum. Only the over-all scale factor $d\sigma_{\rho\omega}/dt$ is free in fitting the experimental $\rho\omega$ peak.

The ϕ peak shape is fixed by convoluting a δ function at $m_x^2 = m_\phi^2$ with the experimental resolution. We represent the continuum background as a polynomial in $p^* = (m_x^2/4 - m_\pi^2)^{1/2}$. This variable was chosen to match the phase-space threshold

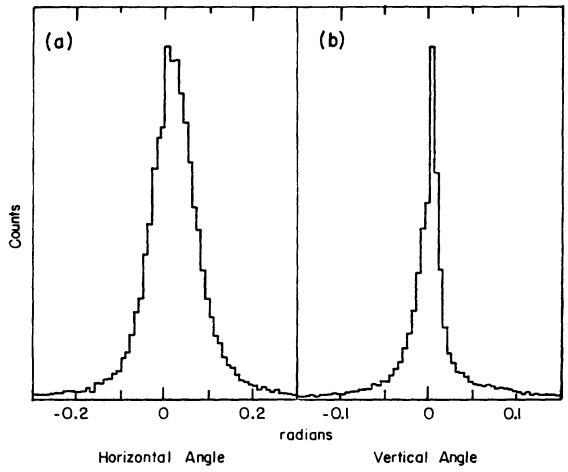

FIG. 13. Distributions in the direction of the missing momentum ($\gamma_v + p \to p + x$) for missing masses near zero: (a) horizontal angle, (b) vertical angle. The peaking in the beam direction is a feature of the bremsstrahlung reaction, but the width of the peak (especially for the horizontal angle) is dominated by experimental resolution

dependence for two-pion production; p^* is the center-of-mass momentum of one pion of the pair. Since the fits over the m_x^2 range up to 1.5 GeV^2 were rather insensitive to higher powers of p^*, the results we present here are obtained with the continuum constrained to be proportional to p^* and with only the magnitude as a free parameter. The continuum yield has a generally flatter t dependence than the ρ^0 and ω production, and is similar to the proton missing-mass continuum in photoproduction.[38] It is presumably a mixture of $\Delta\pi$ and nonresonant $p\pi\pi$ and $p\pi\pi\pi$ final states.

Figure 14 shows the fitted values for the sum of ρ^0 and ω cross sections plotted against t. We fit each t distribution to an exponential form:

$$\frac{d\sigma_{\rho\omega}}{dt} = \frac{d\sigma_{\rho\omega}}{dt}\bigg|_{t=0} e^{Bt}; \tag{5}$$

the results are listed in Table III along with the integrated cross sections $\sigma_{\rho\omega}$ (the exponential fit integrated from $t_{\min}$ to $t_{\max}$). In Fig. 15 we plot the Q^2 dependence of $\sigma_{\rho\omega}/\sigma_{\mathrm{tot}}$, with σ_{tot}, the virtual-photon proton interaction cross section, taken from a fit[39] to the single-arm inelastic electron scattering data. As we have observed in a previous experiment,[18] $\sigma_{\rho\omega}$ drops more rapidly with Q^2 than does σ_{tot}. Virtual photoproduction is apparently becoming less diffractive as the photon becomes more spacelike and its q^2 ($= -Q^2$) gets farther from m_ρ^2 and m_ω^2. Qualitatively, such an effect is predicted by vector-meson dominance. In its simplest form[40] the model says

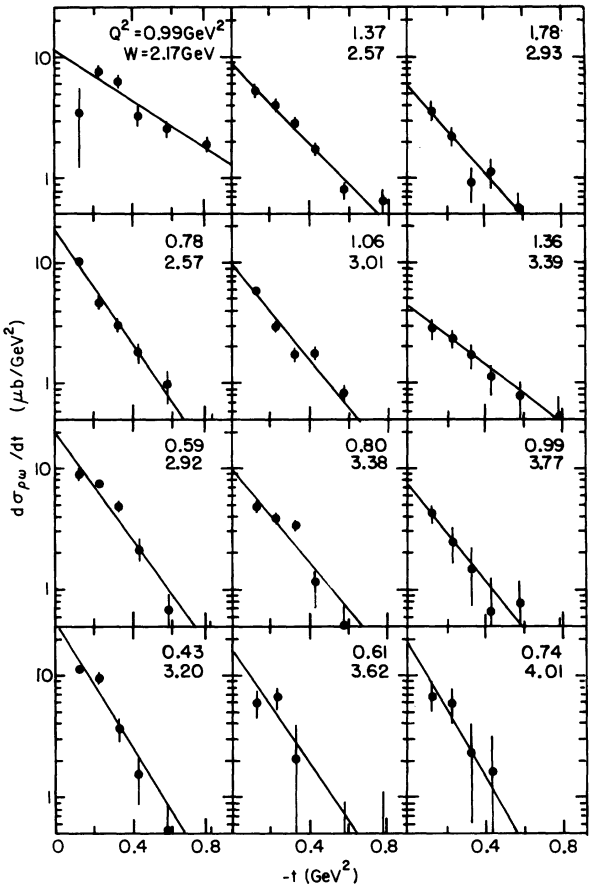

FIG. 14. Differential cross sections for ρ^0 and ω virtual photoproduction as functions of t for the various Q^2 and W values covered in this experiment. The lines show the best exponential fit.

TABLE III. Measured cross sections and slopes for $\gamma_v + p \to p + \rho^0$ or ω. Quoted errors include an estimate of the systematic uncertainties, although the statistical errors dominate.

Q^2 (GeV^2)	W (GeV)	$B_{\rho\omega}$ (GeV^{-2})	$(d\sigma/dt)_{t=0}$ (μb/GeV^2)	$\sigma_{\rho\omega}/\sigma_{\rm tot}$
0.99	2.17	2.7±0.4	14±3	0.075±0.015
0.78	2.57	5.8±0.5	22±3	0.053±0.008
0.59	2.92	5.4±0.6	22±3	0.063±0.008
0.43	3.20	6.3±0.8	31±5	0.072±0.011
1.37	2.57	3.8±0.4	9.4±1.5	0.049±0.008
1.06	3.01	4.8±0.5	9.7±1.8	0.045±0.006
0.80	3.38	4.4±0.9	10±2	0.048±0.006
0.61	3.62	6.4±3.7	16±7	0.045±0.016
2.23	2.39	1.2±1.8	1.1±1.4	0.030±0.041
1.78	2.93	4.8±1.0	7.2±2.5	0.038±0.012
1.36	3.39	3.2±0.6	4.7±0.9	0.043±0.009
0.99	3.77	4.3±1.1	7.4±1.9	0.043±0.011
0.74	4.01	6.4±3.0	17±9	0.058±0.014

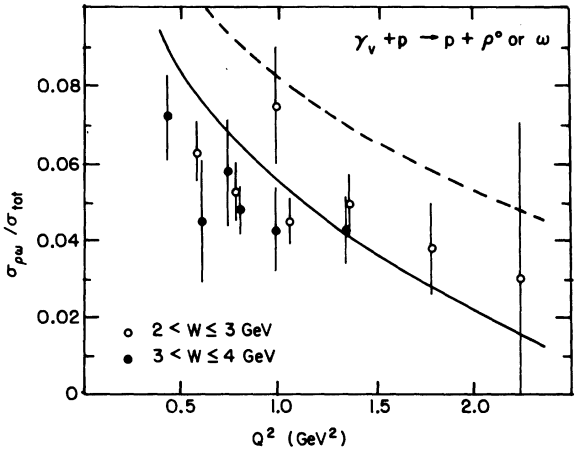

FIG. 15. Measured relative cross section for ρ^0 and ω production plotted against Q^2 for two ranges of W. The curves are predictions of the simple vector-dominance model (see text) with $\xi = 0$ (solid) and $\xi = 0.45$ (dashed), computed for an average W value.

$$\sigma_{\rho\omega}(Q^2, W) = \sigma_{\rho\omega}(0, W)\,\frac{m_\rho^4}{(Q^2+m_\rho^2)^2} \times e^{B(t_{\rm min}-t_{\rm min,0})}\left(1+\xi\,\frac{Q^2}{m_\rho^2}\right). \quad (6)$$

In this picture the decrease relative to the photoproduction cross section comes from the virtual ρ (or ω) propagator factor and from the increase in $t_{\rm min}$ with increasing Q^2:

$$-t_{\rm min} \approx \left(\frac{Q^2+m_\rho^2}{2\nu}\right)^2. \quad (7)$$

The contribution from longitudinally polarized photons is represented by the $\xi Q^2/m_\rho^2$ term. The transverse and longitudinal contributions are not separated in our experiment, but there are indications from other experiments[9,14] in which the ρ^0 decay distribution is observed, that the longitudinal-transverse ratio is consistent with $\xi = 0.45$. The curves in Fig. 15 show the model predictions for $\xi = 0$ and $\xi = 0.45$, again divided by the experimental $\sigma_{\rm tot}$. The model can be made to fit our data only if ξ is essentially zero (it cannot be negative). Since the evidence[9,14] for nonzero ξ is good, this means that this form of the vector-dominance model does not correctly explain the rapid decrease in $\sigma_{\rho\omega}(Q^2)$. The discrepancy cannot be explained as an error in beam and target normalization. Such errors are negligible (see Sec. II), and no such discrepancy showed up in checking the elastic ep scattering yields.

Although there is no compelling evidence in our data for any deviations from a simple exponential in t, it is obvious from Table III that the t-slope parameter $B_{\rho\omega}$ decreases[41] with increasing Q^2.

There is also a tendency at fixed Q^2 for $B_{\rho\omega}$ to increase with increasing W (or ν). This suggests that $B_{\rho\omega}$ may depend only on the ratio Q^2/ν. Since there are indications that $B_{\rho\omega}$ has a similar ν dependence in photoproduction,[42] we are led to consider instead the ratio $(Q^2+b)/\nu$, where b is some positive constant, thus allowing us to relate the variation of $B_{\rho\omega}$ in electroproduction ($Q^2>0$) and in photoproduction ($Q^2=0$). Figure 16 shows a test of the conjecture that $B_{\rho\omega}$ is a function of $x_\rho=(Q^2+m_\rho^2)/2M\nu$, using data from this and other electroproduction experiments,[9,14,17] as well as some photoproduction data.[43] The tendency for the measurements to lie along a simple curve is somewhat more pronounced than when they are plotted against Q^2 (Fig. 17), although the optimum choice for b is somewhat lower than m_ρ^2.

It is not possible with the available data to rule out a more general dependence on two variables: Q^2 and ν, or perhaps Q^2 and x_ρ. For example, as an exercise we have fitted the slope to a form

$$B_{\rho\omega}=B_0\,\frac{1-x_\rho/x_0}{1+Q^2/Q_0^2}\,. \tag{8}$$

The fit is tolerably good, considering the inconsistencies among slope values from different experiments, especially in photoproduction. The best-fit parameters are $B_0=7.8\pm0.2$ GeV^{-2}, $x_0=0.69\pm0.09$, and $Q_0^2=4.2\pm1.6$ GeV^2. Clearly, the data allow a weak Q^2 variation distinct from the strong x_ρ dependence, but the latter makes the former difficult to establish.

It has been suggested[44] that in the vector-meson-dominance picture the effective size of the interaction region in a photon-hadron collision is determined by the lifetime Δt of the virtual hadronic components of the photon. The lifetime is given by the reciprocal of the energy mismatch between the photon and its hadronic components, which in the case of ρ production should presumably be dominated by the ρ. That is

$$\Delta t=[(\nu^2+Q^2+m_\rho^2)^{1/2}-\nu]^{-1}$$
$$\approx 2\nu/(Q^2+m_\rho^2)=(Mx_\rho)^{-1}. \tag{9}$$

Assuming that ρ^0 photoproduction and electroproduction are mainly diffractive, one can argue that the slope of the diffraction peak B_ρ is a measure of the size of the interaction region, and that one should therefore expect to see $B_{\rho\omega}$ decrease with decreasing Δt or increasing x_ρ, as the photon becomes more pointlike. Our data are consistent with such a picture, but the "shrinking photon" model is not the only possible explanation; other mechanisms for Q^2 dependence have been proposed.[45] Several of these effects may be acting together. As pointed out above, the data are compatible with separate dependences on x_ρ and on Q^2, although the former seems to be more important in the kinematic range investigated so far.

Relative to the ρ^0 and ω cross sections, the ϕ cross sections $d\sigma_\phi/dt$ are less accurately determined in the fits to the m_x^2 spectra because of the lower yields for ϕ. Therefore, in order to determine the integrated σ_ϕ, we have fitted to the form

$$\frac{d\sigma_\phi}{dt}=\left.\frac{d\sigma_\phi}{dt}\right|_{t=0} e^{B_\phi t}\,, \tag{10}$$

with B_ϕ fixed at 4 GeV^{-2}, a value near that seen in photoproduction.[42] Averaged over our entire Q^2 range and $W>2.45$ GeV, we find $\sigma_\phi/\sigma_{\rho\omega}=0.023\pm0.005$, which is to be compared with 0.025 ± 0.005 in photoproduction[43] at $W=3.12$ GeV.

VII. PROTON INCLUSIVE RESULTS

The data on the continuum in the proton missing-mass spectrum confirm the conclusions of Lazarus *et al.*[21] Beyond the vector-meson peaks there is no marked m_x^2 dependence in the cross section,

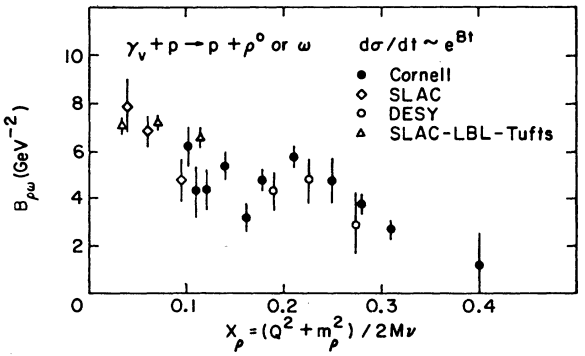

FIG. 16. Measured slope of the t distribution for ρ^0 and ω plotted against $x_\rho=(Q^2+m_\rho^2)/2M\nu$. Diamonds, open circles, and triangles are data from Refs. 14, 9, and 43, respectively.

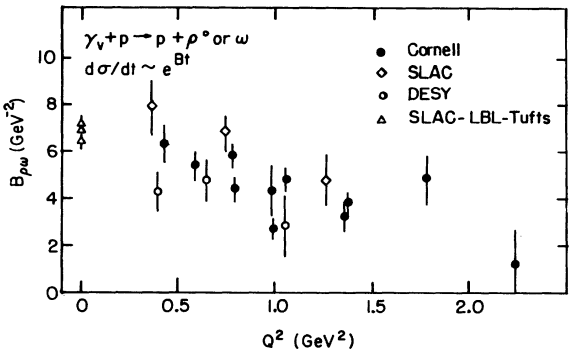

FIG. 17. The data of Fig. 16 plotted against Q^2.

and the slopes in t are uniformly about half of the corresponding slopes in vector-meson production. At high $|t|$ the yield of identifiable two-body states has dropped to a negligible fraction of the total.

To obtain an alternative description of the continuum, we compute the invariant cross section $E\,d\sigma/d^3p$. This is related to the m_x^2 distribution by the simple transformation

$$E\frac{d\sigma}{d^3p} = \frac{2M(\nu^2+Q^2)^{1/2}}{\pi}\frac{d\sigma}{dm_x^2\,dt}. \tag{11}$$

The invariant cross section is customarily described in terms of p_t and $x = p_l/p_{\max}$, where p_l and p_t are the longitudinal and transverse proton momentum components relative to the virtual photon axis in the photon-proton center-of-mass system. However, for convenience we use here

TABLE IV. Experimental results for the inclusive reaction $\gamma_v + p \to p$ + anything. The quantities listed are defined in the text. Data in square brackets are obtained by excluding the contribution from ρ^0 and ω production. The quoted errors include only the statistical uncertainty; the systematic errors are expected to be rather small by comparison.

Q^2 (GeV^2)	W (GeV)	x	B_p (GeV^{-2})	$\frac{E}{\sigma}\frac{d\sigma}{d^3p}\Big\|_{p_t=0}$ (GeV^{-2})	$\left\langle\frac{1}{\sigma}\frac{d\sigma}{dx}\right\rangle$
0.99	2.17	−0.78	1.9 ± 0.1	1.10 ± 0.06	
			[1.0 ± 0.2	0.41 ± 0.04]	
		−0.60	4.4 ± 1.6	0.49 ± 0.10	0.21 ± 0.11
0.78	2.57	−0.86	3.1 ± 0.1	1.45 ± 0.06	
			[1.6 ± 0.1	0.51 ± 0.03]	
		−0.76	3.2 ± 0.3	0.78 ± 0.05	0.58 ± 0.05
		−0.70	3.9 ± 0.5	0.80 ± 0.08	
0.59	2.92	−0.90	4.1 ± 0.2	2.07 ± 0.11	
			[1.9 ± 0.1	0.42 ± 0.03]	
0.43	3.20	−0.92	5.4 ± 0.3	3.46 ± 0.26	
			[2.9 ± 0.2	0.57 ± 0.04]	
		−0.84	4.2 ± 0.3	0.82 ± 0.07	0.58 ± 0.03
		−0.79	3.4 ± 0.4	0.66 ± 0.06	
		−0.75	3.9 ± 0.4	0.84 ± 0.08	
		−0.70	3.3 ± 0.6	0.66 ± 0.09	
		−0.87	5.3 ± 0.5	1.50 ± 0.16	0.68 ± 0.04
		−0.84	5.9 ± 0.6	1.07 ± 0.14	
		−0.80	4.6 ± 0.5	0.95 ± 0.12	
		−0.77	3.6 ± 0.5	0.76 ± 0.10	
		−0.73	4.1 ± 0.6	0.86 ± 0.12	
		−0.70	1.5 ± 1.3	0.55 ± 0.17	
1.37	2.57	−0.86	2.9 ± 0.2	1.25 ± 0.07	
			[1.4 ± 0.2	0.36 ± 0.04]	
		−0.76	2.2 ± 0.5	0.50 ± 0.05	0.49 ± 0.13
		−0.70	1.0 ± 1.3	0.30 ± 0.08	
1.06	3.01	−0.91	3.5 ± 0.2	1.46 ± 0.09	
			[1.9 ± 0.2	0.37 ± 0.03]	
		−0.85	4.2 ± 0.5	0.70 ± 0.07	0.52 ± 0.04
		−0.81	3.4 ± 0.4	0.58 ± 0.06	
		−0.77	3.4 ± 0.4	0.74 ± 0.07	
		−0.73	3.0 ± 0.6	0.56 ± 0.08	
		−0.69	3.2 ± 2.8	0.53 ± 0.28	
0.80	3.38	−0.94	3.6 ± 0.3	1.57 ± 0.15	
			[1.2 ± 0.2	0.20 ± 0.02]	

TABLE IV *(Continued)*

Q^2 (GeV^2)	W (GeV)	x	B_p (GeV^{-2})	$\frac{E}{\sigma}\frac{d\sigma}{d^3p}\Big\|_{p_t=0}$ (GeV^{-2})	$\left\langle \frac{1}{\sigma}\frac{d\sigma}{dx} \right\rangle$
		−0.89	3.0 ± 0.6	0.50 ± 0.10	
		−0.86	1.6 ± 0.6	0.31 ± 0.07	
		−0.83	2.7 ± 0.7	0.43 ± 0.08	0.52 ± 0.06
		−0.80	1.6 ± 0.7	0.35 ± 0.07	
		−0.77	3.1 ± 0.6	0.57 ± 0.09	
		−0.74	3.3 ± 1.1	0.54 ± 0.14	
0.61	3.62	−0.94	6.3 ± 1.0	3.45 ± 0.73	
			[3.5 ± 0.9	0.37 ± 0.09]	
		−0.91	6.1 ± 1.9	1.27 ± 0.49	
		−0.88	4.0 ± 1.9	0.61 ± 0.30	
		−0.86	5.3 ± 2.0	0.85 ± 0.34	0.43 ± 0.09
		−0.83	5.3 ± 2.8	0.52 ± 0.29	
		−0.81	5.2 ± 3.0	0.54 ± 0.29	
		−0.78	3.5 ± 2.0	0.60 ± 0.28	
2.23	2.39	−0.94	1.9 ± 0.5	0.81 ± 0.22	
			[2.9 ± 1.4	0.53 ± 0.34]	
1.78	2.93	−0.91	3.4 ± 0.4	1.25 ± 0.14	
			[0.5 ± 0.9	0.29 ± 0.06]	
		−0.84	3.0 ± 1.0	0.44 ± 0.10	
		−0.80	3.1 ± 1.3	0.46 ± 0.14	0.41 ± 0.11
		−0.76	0.7 ± 2.3	0.24 ± 0.13	
1.36	3.39	−0.94	3.1 ± 0.4	1.40 ± 0.16	
			[2.0 ± 0.3	0.29 ± 0.04]	
		−0.89	2.7 ± 0.8	0.50 ± 0.11	
		−0.86	5.4 ± 1.8	0.60 ± 0.18	
		−0.84	4.9 ± 1.4	0.64 ± 0.16	0.44 ± 0.06
		−0.78	3.9 ± 1.1	0.66 ± 0.16	
		−0.75	2.2 ± 1.6	0.45 ± 0.18	
0.99	3.77	−0.95	4.5 ± 0.6	2.29 ± 0.04	
			[3.4 ± 0.6	0.29 ± 0.07]	
		−0.92	2.3 ± 1.0	0.53 ± 0.18	
		−0.89	2.9 ± 1.3	0.40 ± 0.17	
		−0.87	5.1 ± 1.1	1.07 ± 0.25	0.52 ± 0.08
		−0.85	5.1 ± 2.1	0.75 ± 0.28	
		−0.83	4.7 ± 2.2	0.59 ± 0.24	
		−0.81	4.8 ± 1.8	0.79 ± 0.28	

$$x = [1 + (p_t/p_l)^2]^{1/2} p_l / p_{\max} \qquad (12)$$

instead of the more usual definition; the numerical difference is not significant in our range of p_l and p_t.

We fit the invariant cross section at fixed x to the form

$$E\frac{d\sigma}{d^3p} = \left(E\frac{d\sigma}{d^3p}\right)_{p_t=0} e^{-Bp_t^2}, \qquad (13)$$

and calculate the integral over transverse momenta

$$\frac{d\sigma}{dx} = \pi p_{\max} \int \left(E\frac{d\sigma}{d^3p}\right)\frac{dp_t^2}{E} . \qquad (14)$$

The results are given in Table IV. No radiative correction has been made.

For several of the Q^2, W points covered in this experiment there exist extensive data[13] on the

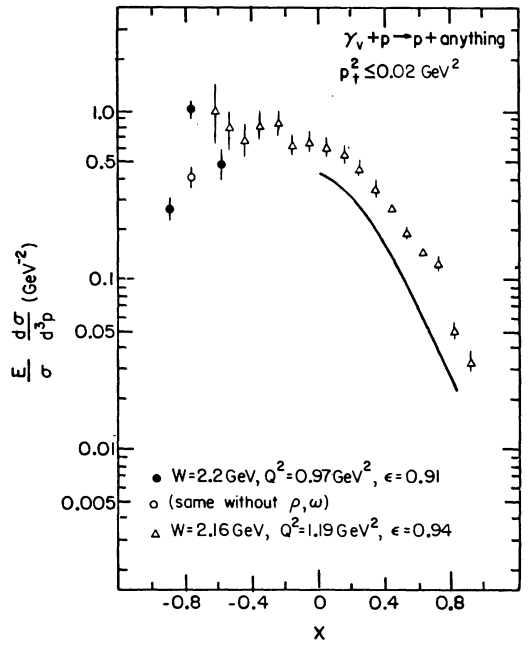

FIG. 18. Invariant cross section for $\gamma_v + p \to p$ +anything. Solid circles are our data; open circles are our data excluding ρ^0 and ω production (ρ^0 and ω contribute to only one x bin); triangles are data from Ref. 13; the curve follows the trend of photoproduction data at W =2.5 GeV (Ref. 6).

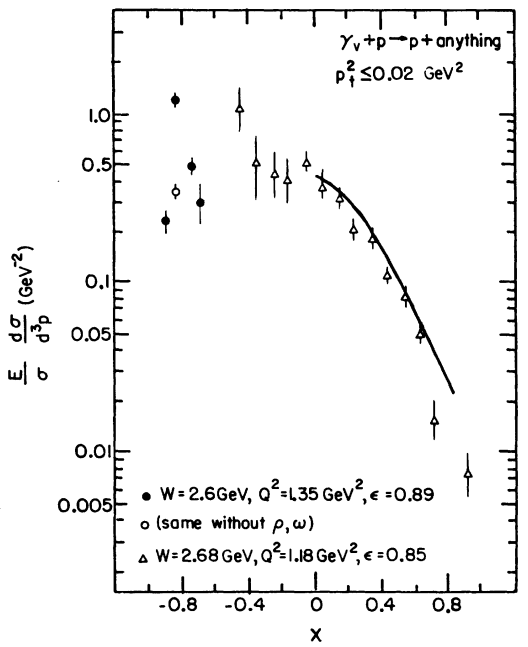

FIG. 20. Invariant cross section for $\gamma_v + p \to p$ +anything. Solid circles are our data; open circles are our data excluding ρ^0 and ω production; triangles are data from Ref. 13; the curve follows the trend of photoproduction data at W =2.5 GeV (Ref. 6).

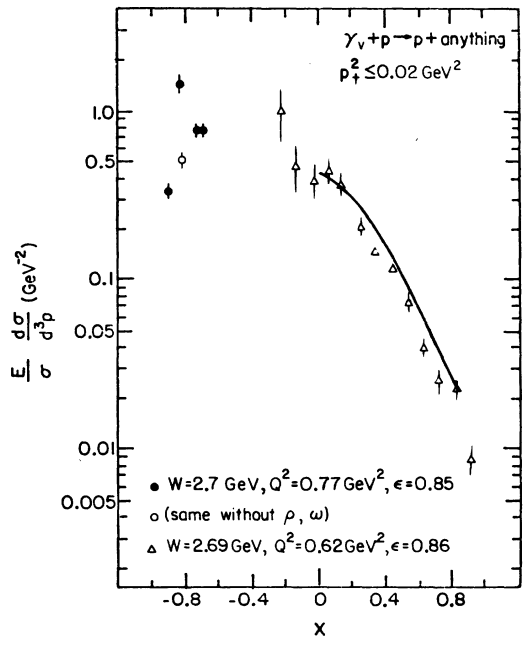

FIG. 19. Invariant cross section for $\gamma_v + p \to p$ +anything. Solid circles are our data; open circles are our data excluding ρ^0 and ω production; triangles are data from Ref. 13; the curve follows the trend of photoproduction data at W =2.5 GeV (Ref. 6).

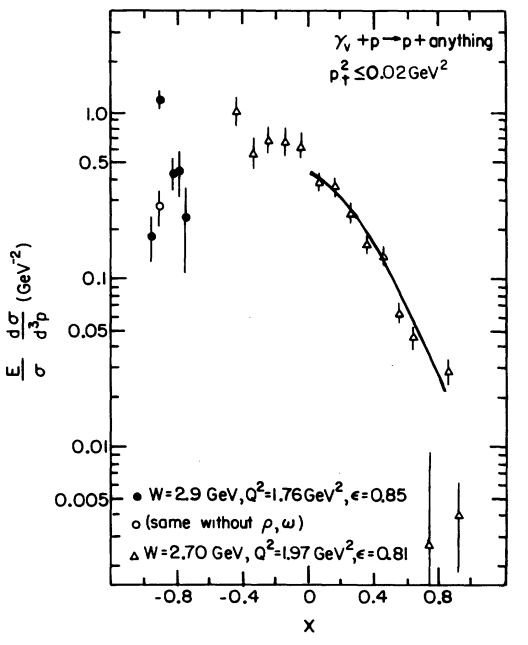

FIG. 21. Invariant cross section for $\gamma_v + p \to p$ +anything. Solid circles are our data; open circles are our data excluding ρ^0 and ω production; triangles are data from Ref. 13; the curve follows the trend of photoproduction data at W =2.5 GeV (Ref. 6).

proton inclusive cross section at zero p_t in the forward ($x>0$) hemisphere. Figures 18–21 show how these data are supplemented by our backward proton data. In each case one notes a leading-particle peak near $x=-1$ corresponding to the vector-meson channels such as $\gamma_v + p \to p + \rho$, then a slowly varying yield in the rest of the backward hemisphere, and then a rapid falloff in the forward hemisphere. The only changes in the normalized invariant cross section $(E/\sigma)(d\sigma/d^3p)_{p_t=0}$ as Q^2 and W are varied are (a) the disappearance of the vector-meson peak at high Q^2 (discussed above in Sec. VI), (b) a decrease in the forward yield at higher W (noted in Ref. 13), and (c) a gradual decrease in the backward hemisphere plateau with increasing Q^2.

The latter effect is seen more clearly in Fig. 22, where we plot $(1/\sigma)(d\sigma/dx)$ averaged over the x range of our experimental acceptance, but excluding the portion near $x=-1$ dominated by the ρ^0 and ω channels. The backward plateau yield has little or no dependence on W, but appears to decrease with Q^2. The integral over x is just the average proton multiplicity, or probability per collision that the final-state baryon will be a proton (rather than a neutron or hyperon):

$$\bar{n}_p = \int_{-1}^{1} \frac{1}{\sigma}\frac{d\sigma}{dx}\,dx = \pi p_{\max}\int\left(E\frac{d\sigma}{d^3p}\right)\frac{dp_t^{\,2}}{E}\,. \qquad (15)$$

To get a first approximation to the integral, we can neglect the forward-hemisphere yield and the vector-meson peak, and assume that our measured $(1/\sigma)(d\sigma/dx)$ is typical of the backward hemisphere ($x=-1$ to 0). Then the data plotted in Fig. 22 can be viewed as a measure of $\bar{n}_p$ as a function of Q^2. The mean proton multiplicity in photoproduction ($Q^2=0$, $W=3$ GeV) has been estimated[46] at 0.7, and our data indicate (Fig. 22) that it decreases in electroproduction. One therefore would expect an increasing yield of neutrons (and/or hyperons) as Q^2 increases. Such an effect has been observed[31,47] for neutrons. One should also expect to see an increase in the yield of π^+ relative to π^-, in order to maintain charge balance as the proton yield decreases. This has also been observed, not only for pions emitted in the forward hemisphere[13,14] but also for pions in the central region (see Sec. VIII below).

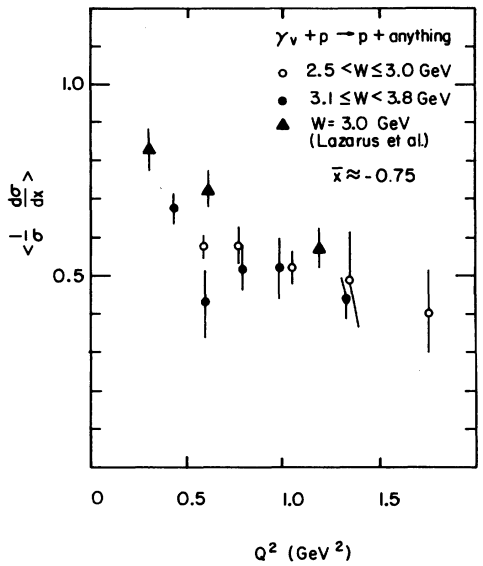

FIG. 22. The inclusive cross section $(1/\sigma)(d\sigma/dx)$ for $\gamma_v + p \to p +$anything, integrated over p_t and averaged over the range of x corresponding to the backward hemisphere plateau (see text), plotted against Q^2 for two ranges of W. Triangles are data from Ref. 21.

VIII. PION INCLUSIVE RESULTS

There are four categories of electron-pion coincidence data in this experiment: π^+ and π^- with the hadron magnet polarity set to bend π^+ to larger angles, and π^- and π^+ with the magnet bending π^- to larger angles. The bulk of the running time was devoted to the former polarity condition, and the angular acceptance was greater for particles bent to backward angles. Consequently, the most complete data exist for the π^+ yield in the backward-bend condition. We therefore present absolute cross sections only for this preferred category of data, and use all categories only to derive π^+/π^- yield ratios.

For each data category and for each of the E, ω' bins (Fig. 6 and Table I) we further subdivide the electron-pion data into bins in x and $p_t^{\,2}$. In this case we define the longitudinal variable as $x = p_l/(p_{\max}^{\,2} - p_t^{\,2})^{1/2}$. Since $p_t/p_{\max}$ is always small, the distinction between our definition and the more conventional one is insignificant. In the case of data used for π^+ cross sections[28] the observed yield in each bin is corrected for efficiencies and pion decay, divided by the incident electron number, target density, bin widths $\Delta x \Delta p_t^{\,2}$, virtual-photon flux factor Γ, and geometric acceptance. Otherwise, the data are simply divided by the appropriate incident electron number before forming the ratio with data for the opposite magnet polarity and opposite pion charge; all other factors cancel in the ratio.

The invariant cross sections (averaged over ϕ)

$$E\frac{d\sigma}{d^3p} = \frac{E}{\pi p_{\max}}\frac{d\sigma}{dx\,dp_t^{\,2}}, \qquad (16)$$

TABLE V. Experimental results for the inclusive reaction $\gamma_v + p \to \pi^+ +$ anything. The quantities listed are defined in the text. The quoted errors include only the statistical uncertainty; the systematic errors are expected to be rather small by comparison.

Q^2 (GeV^2)	W (GeV)	x	B_π (GeV^{-2})	$\frac{E}{\sigma}\frac{d\sigma}{d^3p}\Big\vert_{p_t=0}$ (GeV^{-2})	$F(x)$
1.26	2.10	−0.1	5.0 ± 2.1	0.37 ± 0.11	
		0	13.5 ± 1.7	1.06 ± 0.11	0.084 ± 0.008
		0.1	8.6 ± 1.2	0.80 ± 0.10	
		0.2	8.2 ± 1.7	0.74 ± 0.12	
0.99	2.17	−0.1	10.4 ± 0.9	0.75 ± 0.07	
		0	11.0 ± 1.1	0.83 ± 0.09	0.075 ± 0.005
		0.1	11.5 ± 1.8	1.09 ± 0.24	
0.78	2.57	−0.1	11.0 ± 1.0	0.95 ± 0.07	0.094 ± 0.005
		0	9.0 ± 0.8	0.91 ± 0.06	
0.59	2.92	−0.2	8.0 ± 1.9	0.49 ± 0.12	
		−0.1	10.4 ± 0.9	1.01 ± 0.08	0.097 ± 0.009
0.43	3.20	−0.2	10.0 ± 2.2	0.74 ± 0.21	
		−0.1	8.0 ± 1.5	0.70 ± 0.09	0.087 ± 0.015
1.61	2.19	−0.2	7.7 ± 2.0	0.53 ± 0.16	
		−0.1	10.1 ± 1.2	0.92 ± 0.10	0.099 ± 0.008
		0	8.4 ± 1.0	0.92 ± 0.08	
1.37	2.57	−0.2	13.4 ± 2.6	0.96 ± 0.30	
		−0.1	9.0 ± 1.0	0.90 ± 0.08	0.104 ± 0.015
		0	10.1 ± 1.3	1.10 ± 0.10	
1.06	3.01	−0.2	10.6 ± 2.0	0.88 ± 0.22	
		−0.1	6.4 ± 0.8	0.86 ± 0.07	0.134 ± 0.015
0.80	3.38	−0.2	5.5 ± 1.9	0.45 ± 0.14	
		−0.1	9.3 ± 1.6	1.12 ± 0.12	0.131 ± 0.019
0.61	3.62	−0.2	4.1 ± 3.4	0.44 ± 0.25	
2.23	2.39	−0.2	7.4 ± 3.2	0.51 ± 0.22	
		−0.1	9.0 ± 1.5	1.00 ± 0.13	0.108 ± 0.013
		0	13.3 ± 2.5	1.39 ± 0.30	
1.78	2.93	−0.2	10.5 ± 2.9	0.80 ± 0.28	
		−0.1	7.7 ± 1.1	0.90 ± 0.10	0.117 ± 0.017
1.36	2.93	−0.2	9.0 ± 2.2	0.74 ± 0.21	
		−0.1	9.4 ± 1.4	1.14 ± 0.11	0.121 ± 0.018
0.99	3.77	−0.2	2.4 ± 2.5	0.32 ± 0.14	
0.74	4.01	−0.2	9.0 ± 3.8	1.11 ± 0.55	

for the inclusive reaction $\gamma_v + p \to \pi^+ +$ anything, are fitted to an exponential in p_t^2:

$$E\frac{d\sigma}{d^3p} = \left(E\frac{d\sigma}{d^3p}\right)_{p_t=0} e^{-Bp_t^2}. \tag{17}$$

The results are given in Table V. No radiative correction has been made. Figures 23–26 show how the available forward-hemisphere $p_t = 0$ data[13] are supplemented by our backward π^+ data. The normalized invariant cross section peaks near $x = 0$. The slope B_π of the p_t^2 dependence shows no systematic dependence on x in our data range; averaged over $0.5 < Q^2 < 1.5$ GeV^2 and $2.4 < W < 3.4$ GeV, we have $B_\pi(x) = 8.8 \pm 0.9$, 8.9 ± 0.4, and 9.3 ± 0.6 GeV^{-2} for $x = -0.2$, -0.1, and 0. Averaged over x from -0.25 to 0.15, $B_\pi(Q^2, W)$ is generally consistent with 9 GeV^{-2}

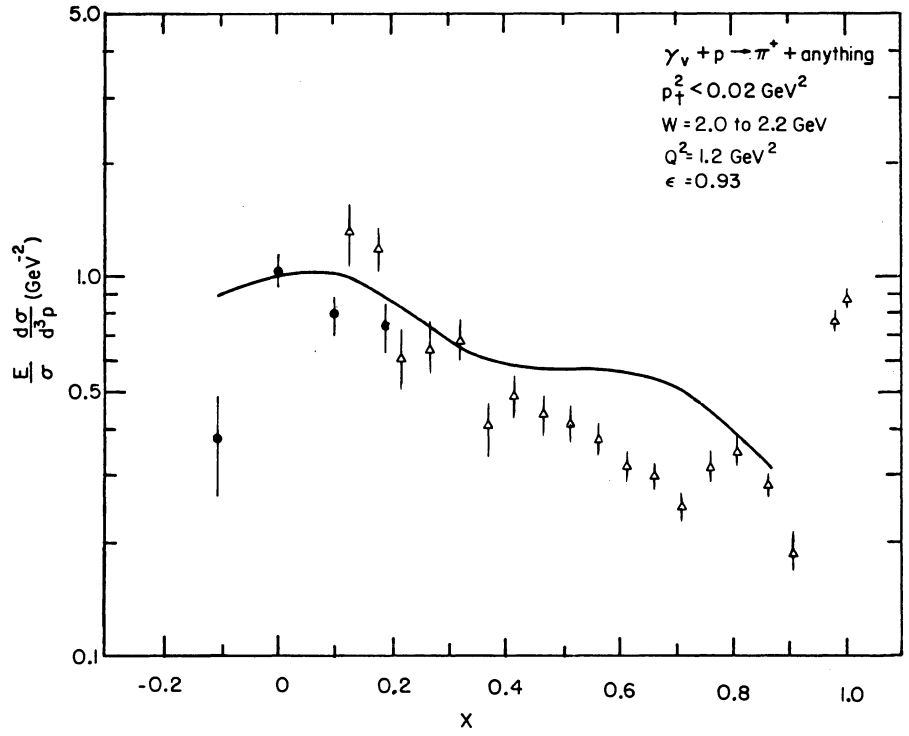

FIG. 23. Invariant cross section for $\gamma_v + p \rightarrow \pi^+ +$anything. Solid circles are our data; triangles are data from Ref. 13. The curve follows the trend of photoproduction data at $W = 2.5$ GeV (Ref. 6).

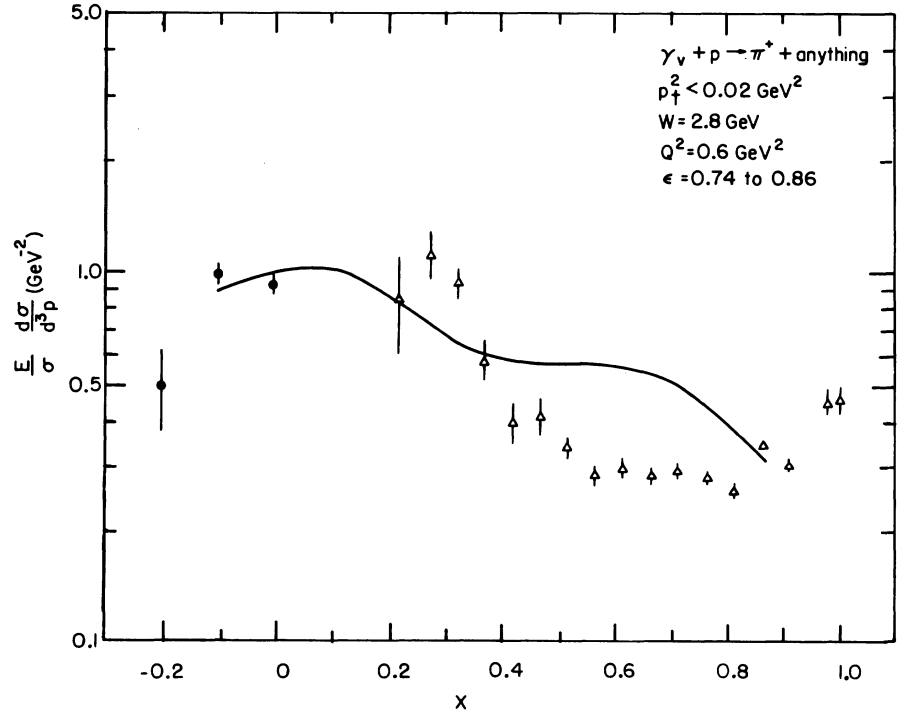

FIG. 24. Invariant cross section for $\gamma_v + p \rightarrow \pi^+ +$anything. Solid circles are our data (two Q^2, W data sets averaged); triangles are data from Ref. 13; the curve follows the trend of photoproduction data at $W = 2.5$ GeV (Ref. 6).

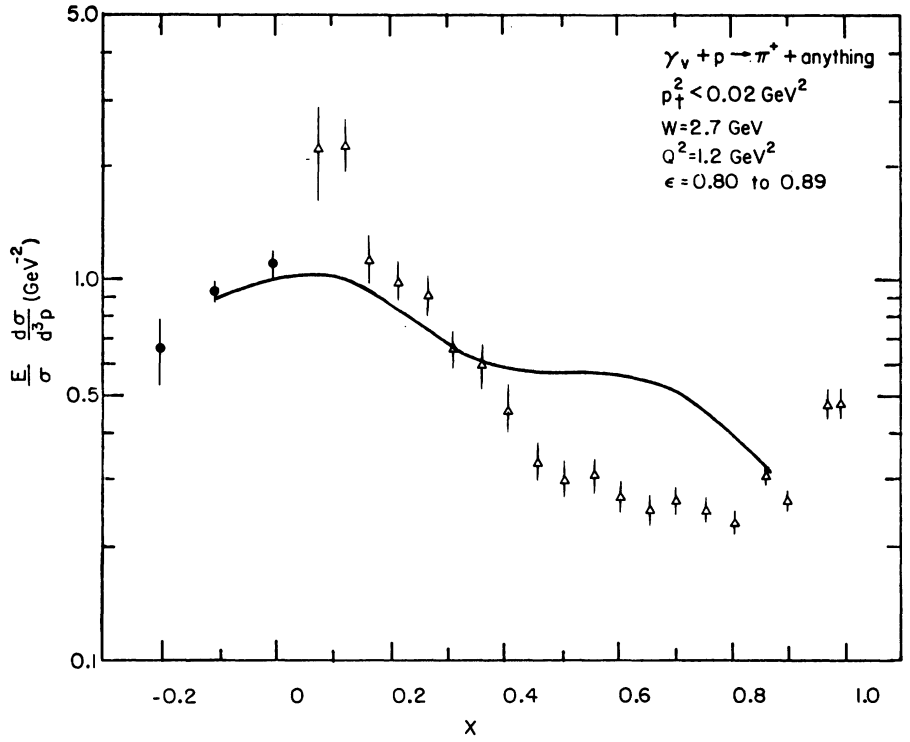

FIG. 25. Invariant cross section for $\gamma_v + p \rightarrow \pi^+ +$anything. Solid circles are our data (two Q^2, W data sets averaged); triangles are data from Ref. 13; the curve follows the trend of photoproduction data at $W = 2.5$ GeV (Ref. 6).

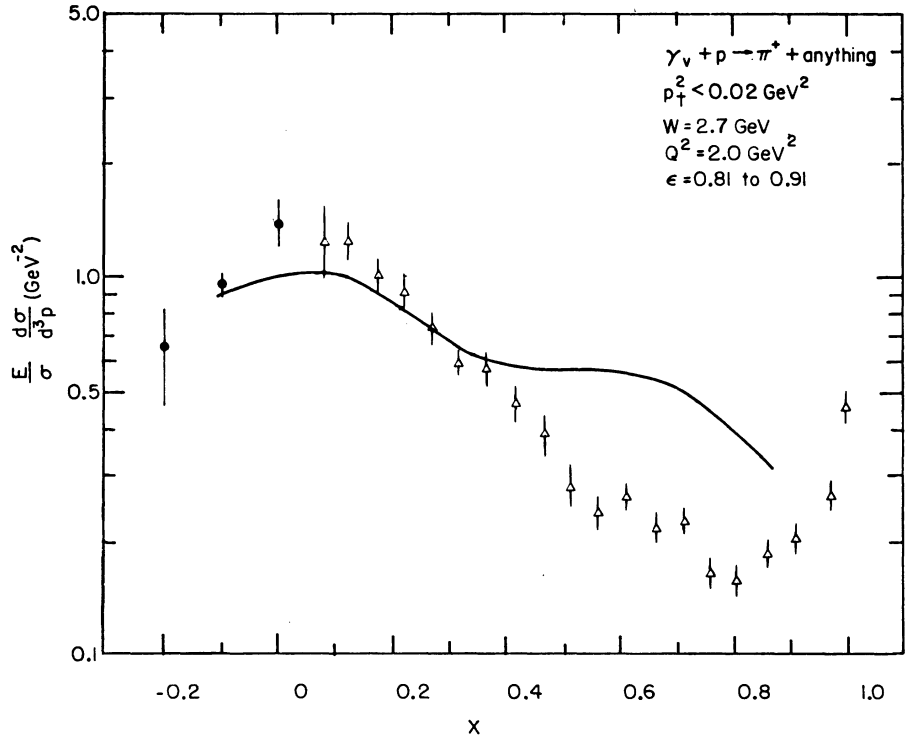

FIG. 26. Invariant cross section for $\gamma_v + p \rightarrow \pi^+ +$ anything. Solid circles are our data (two Q^2, W data sets averaged); triangles are data from Ref. 13; the curve follows the trend of photoproduction data at $W = 2.5$ GeV (Ref. 6).

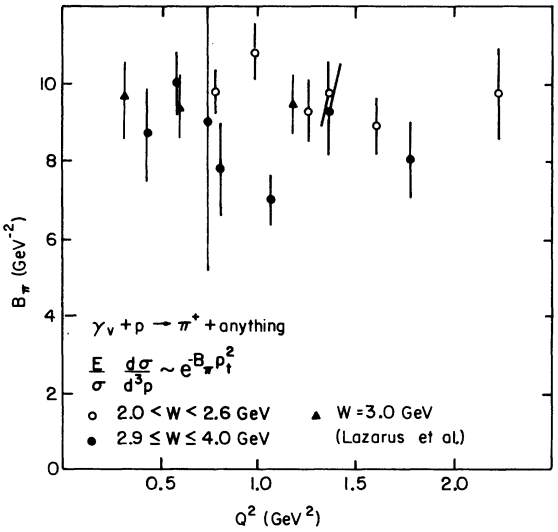

FIG. 27. Slope of the transverse momentum distribution for the inclusive reaction $\gamma_v + p \to \pi^+ +$anything, averaged over the x range of our experiment, plotted against Q^2 for two ranges of W. Triangles are data from Ref. 20.

over the entire range of our data (see Fig. 27). This confirms the conclusion of Lazarus *et al.*,[20] and is in contrast with the tendency for B_π to decrease with increasing Q^2 for pions emitted forward[13,14] ($x > 0.5$).

The integral over transverse momenta

$$F(x) = \int \frac{E}{\sigma}\frac{d\sigma}{d^3p}\, dp_t^2 \ , \tag{18}$$

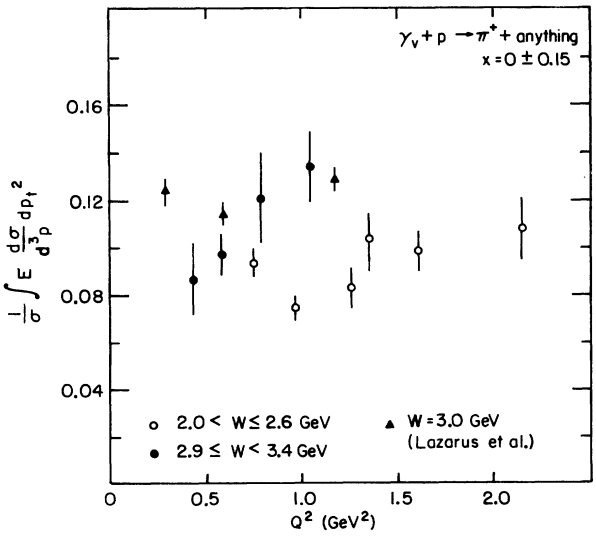

FIG. 28. Invariant cross section for $\gamma_v + p \to \pi^+ +$anything, integrated over p_t and averaged over $|x| < 0.15$, plotted against Q^2 for two ranges of W. Triangles are data from Ref. 20.

TABLE VI. Experimental results for the π^+/π^- yield ratio at an average $x = -0.1$ in the reaction $\gamma_v + p \to \pi^\pm +$ anything. The quantities listed are identified in the text. The quoted errors include only the statistical uncertainty; the systematic errors are expected to be negligible.

Q^2 (GeV^2)	W (GeV)	$B_+ - B_-$ (GeV^{-2})	A^+/A^-	N^+/N^-
0.99	2.17	•••	1.8±0.8	1.6±0.7
0.78	2.57	1.2±3.2	1.1±0.3	1.0±0.3
0.59	2.92	2.6±2.0	1.5±0.5	1.4±0.4
0.43	3.20	1.5±0.9	0.9±0.8	0.8±0.7
1.61	2.19	1.8±1.6	1.8±0.3	1.7±0.3
1.37	2.57	2.8±1.7	1.4±0.2	1.3±0.2
1.06	3.01	1.2±1.3	1.6±0.2	1.5±0.2
0.80	3.38	1.3±1.6	1.4±0.2	1.2±0.2
0.61	3.62	1.2±1.4	1.5±0.6	1.3±0.6

averaged over our data in the central region $|x| < 0.15$, shows a tendency to increase with Q^2 and with W (Fig. 28). The increase with Q^2 is consistent with the results of Lazarus *et al.*[20]; the increase with W has been seen in photoproduction[43] and is a manifestation of the increase in multiplicity with increasing center-of-mass energy. The apparent increase in pion multiplicity with Q^2 at fixed W does not actually contradict other evidence[32] that the over-all charged multiplicity does not increase with Q^2; it may be compensated by the decrease in proton multiplicity noted in Sec. VII.

The data on the pion charge ratio are fitted to the same exponential form,

$$N^+/N^- = (A^+/A^-)\, e^{-\Delta B p_t^2} \ , \tag{19}$$

where A^+/A^- is the π^+/π^- ratio at $p_t = 0$ and $\Delta B = B_+ - B_-$. The results are listed in Table VI. In Fig. 29 we show a typical x distribution of A^+/A^-, including forward-hemisphere data from

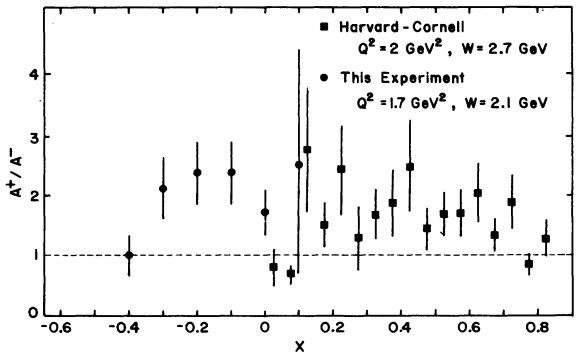

FIG. 29. Ratio of inclusive π^+ and π^- yields at $p_t = 0$, plotted against x for a typical Q^2 and W. Circles are our data; squares are data from Ref. 13.

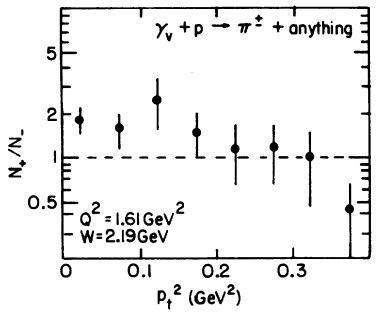

FIG. 30. Ratio of inclusive π^+ and π^- yields, averaged over the x range of our experiment, plotted against p_t^2, for a typical Q^2 and W.

Ref. 13. Our data show that the strong predominance of π^+ over π^- noted in forward electroproduction experiments[13,14] is not a "current fragmentation" phenomenon as previously supposed,[48] but a general feature of the final state, extending to the backward hemisphere as well. It is hard to know whether to take seriously the apparent dip in the π^+/π^- ratio near $x=0$ in Fig. 29. Moving away from $p_t=0$, however, the picture changes. Over the range of our data ΔB is always positive and consistent with $\Delta B \approx 2\ \mathrm{GeV}^{-2}$, implying that the π^- transverse momentum distribution is less steep $[\exp(-7p_t^2)]$ than the π^+ distribution $[\exp(-9p_t^2)]$. For $p_t^2 > 0.4$ GeV the π^- yield actually dominates (see Fig. 30, for example). No such effect has been noted in previous experiments,[14,43] covering mainly the forward hemisphere. The explanation remains a challenge. However, since most of the yield comes from small p_t, the over-all ratio N^+/N^- remains large in our data, and even shows a tendency to increase with Q^2 (Fig. 31).

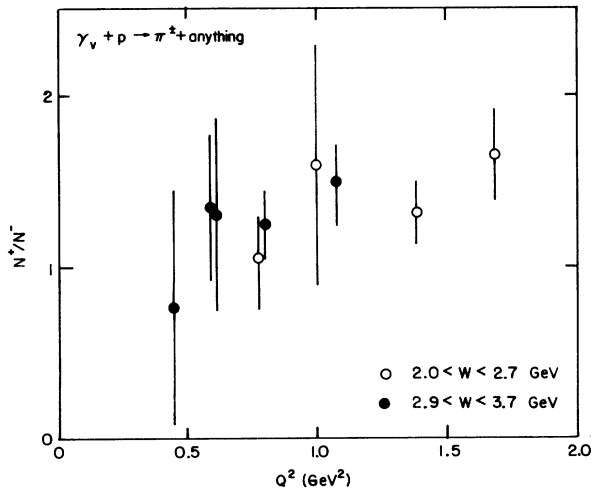

FIG. 31. Ratio of inclusive π^+ and π^- yields, averaged over the x and p_t range of our experiment, plotted against Q^2 for two ranges of W.

One can, of course, compute the average pion charge ratio R, integrated over all p_t and p_t, from the mean charged hadron multiplicity n_{ch} and the mean proton multiplicity n_p, if one ignores strange-particle production. From the definitions $n_{ch} = n_+ + n_- + n_p$ and $R = n_+/n_-$, and the requirement of charge conservation $1 = n_p + n_+ - n_-$, we get $R = (n_{ch} - 2n_p + 1)/(n_{ch} - 1)$. Table VII lists for several Q^2 and W the known values[8,9,32,43] of n_{ch}, corresponding estimates for n_p (Ref. 46 and Sec. VII above), and the implied value of R. An increase in the over-all π^+/π^- ratio with increasing Q^2 of the same order as that observed in this and other experiments is actually compatible with charge conservation. It is not necessary to invoke a variation in the charge ratio with x, although some dependence on x, especially near $x=0$, is not ruled out by the data.

IX. SUMMARY

The important findings of this experiment are the following:

(1) Vector-meson production decreases with Q^2 more rapidly than does the total $\gamma_v + p$ cross section, more rapidly even than the prediction of simple vector-meson dominance.

(2) The slope of the t distribution in ρ^0 and ω production becomes flatter with increasing Q^2 and seems to be at least approximately a function of the single scaling variable $x_\rho = (Q^2 + m_\rho^2)/2M\nu$.

(3) The fraction of final states containing a proton decreases with increasing Q^2.

(4) In the central region, as well as in the forward region of longitudinal momenta, the inclusive π^+ yield seems to increase relative to the π^- yield as Q increases.

(5) The average transverse momentum of π^- is greater than that of π^+ in the x range -0.5 to $+0.1$.

TABLE VII. Measured charged-hadron and proton multiplicities for several Q^2 and W values, with over-all π^+/π^- yield ratios calculated from the multiplicities (see text for formula).

Q^2 (GeV^2)	W (GeV)	n_{ch}	n_p	$R = \pi^+/\pi^-$
0	3.1	3.07 ± 0.10[a]	0.7 ± 0.1[b]	1.29 ± 0.10
1.4	2.9	2.71 ± 0.08[c]	0.44 ± 0.06[d]	1.65 ± 0.12
2.4	3.1	2.89 ± 0.05[c]	0.3 ± 0.1[d]	1.74 ± 0.12

[a] From Ref. 43.
[b] Estimated from Ref. 46.
[c] From Ref. 32.
[d] Estimate based on the data plotted in Fig. 23.

*Work supported by the National Science Foundation.

†Present address: Bell Telephone Laboratories, Murray Hill, New Jersey 07971.

‡On leave 1973–74 at Physikalisches Institut der Universität, Bonn, Germany.

§Present address: Physics Dept. University of Illinois, Urbana, Illinois 60181.

‖Present address: Physics Dept., University of Michigan, Ann Arbor, Michigan 48104.

¶Present address: Mitre Corporation, Boston, Massachusetts.

[1]G. Miller *et al.*, Phys. Rev. D 5, 528 (1972).

[2]The total energy W of the final-state hadrons in their center-of-mass system is defined by $W^2 = M^2 - Q^2 + 2M\nu$, where M is the target nucleon mass, ν is the electron energy loss $E - E'$ in the laboratory, and Q^2 (a positive quantity) is the spacelike four-momentum-squared transferred by the electron. In terms of the laboratory electron energies and scattering angle θ_e, $Q^2 = -q^2 = 2EE'(1 - \cos\theta_e)$.

[3]Scaling in $\omega = 2M\nu/Q^2$: J. D. Bjorken, Phys. Rev. 179, 1547 (1969). Scaling in $\omega' = 1 + W^2/Q^2$: E. D. Bloom and F. J. Gilman, Phys. Rev. D 4, 2901 (1971).

[4]J. D. Bjorken and E. A. Paschos, Phys. Rev. 185, 1975 (1969); R. P. Feynman, *Photon-Hadron Interactions* (Benjamin, New York, 1972).

[5]See, for example, J. J. Sakurai and D. Schildknecht, Phys. Lett. 40B, 121 (1972); 41B, 489 (1972); 42B, 216 (1972).

[6]For the most recent review of inclusive experiments, see F. Brasse, in Proceedings of the International Symposium on Electron and Photon Interactions at High Energies, Bonn, 1973 (unpublished).

[7]For the most recent review of exclusive experiments, see R. Talman, in Proceedings of the International Symposium on Electron and Photon Interactions at High Energies, Bonn, 1973 (unpublished).

[8]J. Ballam *et al.*, report contributed to the International Symposium on Electron and Photon Interactions at High Energies, Bonn, 1973 (unpublished). See also E. D. Bloom, in *Proceedings of the XVI International Conference on High Energy Physics, Chicago-Batavia, Ill., 1972,* edited by J. D. Jackson and A. Roberts (NAL, Batavia, Ill., 1973), Vol. 2, p. 66.

[9]V. Eckardt *et al.*, report contributed to the International Symposium on Electron and Photon Interactions at High Energies, Bonn, 1973 (unpublished). See also V. Eckardt *et al.*, Nucl. Phys. B55, 45 (1973).

[10]C. N. Brown *et al.*, Phys. Rev. D 8, 92 (1973); Phys. Rev. Lett. 27, 536 (1971); 27, 1611 (1971); 28, 1086 (1972).

[11]C. Driver *et al.*, Nucl. Phys. B30, 245 (1971); B33, 84 (1972); B38, 1 (1972); B39, 106 (1972); I. Dammann *et al.*, *ibid.* B54, 381 (1973).

[12]J. C. Alder *et al.*, Nucl. Phys. B46, 415 (1972).

[13]C. J. Bebek *et al.*, Phys. Rev. Lett. 30, 624 (1973); 32, 21 (1974); 32, 27 (1974); and reports contributed to the International Symposium on Electron and Photon Interactions at High Energies, Bonn, 1973 (unpublished).

[14]J. T. Dakin *et al.*, Phys. Rev. Lett. 29, 746 (1972); Phys. Rev. D 8, 687 (1973).

[15]E. D. Bloom *et al.*, Phys. Rev. Lett. 28, 516 (1972).

[16]A. Sofair *et al.*, Nucl. Phys. B42, 369 (1972).

[17]R. Talman *et al.*, data presented in the review by R. Talman, Ref. 7.

[18]D. E. Andrews *et al.*, Phys. Rev. Lett. 26, 864 (1971).

[19]D. E. Andrews *et al.*, data presented in the review by K. Berkelman, in *Proceedings of the 1971 International Symposium on Electron and Photon Interactions at High Energies,* edited by N. B. Mistry (Laboratory of Nuclear Studies, Cornell University, Ithaca, New York, 1972).

[20]E. Lazarus *et al.*, Phys. Rev. Lett. 29, 743 (1972).

[21]E. Lazarus *et al.*, Phys. Rev. Lett. 29, 1409 (1972).

[22]L. Ahrens *et al.*, Phys. Rev. Lett. 31, 131 (1973).

[23]J. W. DeWire, Cornell Report No. CLNS-104 (unpublished).

[24]D. E. Andrews, Ph.D. thesis, Cornell University, 1972 (unpublished).

[25]We are indebted to F. M. Pipkin and the Harvard visiting group at the Cornell synchrotron for their generous loan of the electron spectrometer system.

[26]For further details see J. L. Hartmann, Ph.D. thesis, Cornell University, 1973 (unpublished).

[27]For further details see G. S. Brown, Ph.D. thesis, Cornell University, 1973 (unpublished).

[28]For further details see R. C. Rohlfs, Ph.D. thesis, Cornell University, 1973 (unpublished).

[29]For further details see E. Terray, M.S. thesis, Cornell University, 1973 (unpublished).

[30]L. N. Hand, Phys. Rev. 129, 1834 (1964).

[31]L. Ahrens *et al.* (unpublished). This experiment was an investigation of the inclusive reactions $e + p \to e + p$ + anything and $e + p \to e + n$ + anything, using the neutron hodoscope shown in Fig. 1, and performed in parasite mode with the experiment reported here.

[32]P. H. Garbincius *et al.*, Phys. Rev. Lett. 32, 328 (1974).

[33]L. W. Mo and Y. S. Tsai, Rev. Mod. Phys. 41, 205 (1969).

[34]J. D. Jackson, Nuovo Cimento 34, 1644 (1964). We use $m_\rho = 0.765$ GeV and $\Gamma_0 = 0.143$ GeV.

[35]M. Ross and L. Stodolsky, Phys. Rev. 149, 1172 (1966). The Q^2 and t dependence used here was suggested by D. R. Yennie (private communication).

[36]The ω/ρ^0 ratio in photoproduction decreases with W, approaching 15% at high W [J. Ballam *et al.*, Phys. Rev. D 5, 545 (1972); 7, 3150 (1973)]. The meager electroproduction data on the ratio [K. C. Moffeit, in Proceedings of the International Symposium on Electron and Photon Interactions at High Energies, Bonn, 1973 (unpublished)] are consistent with photoproduction. Our results for the combined ρ^0 and ω production cross sections are rather insensitive to the assumed ratio.

[37]A. Bartl and P. Urban, Acta Phys. Aust. 24, 139 (1966). We are indebted to C. Lichtenstein for a computer program.

[38]G. E. Gladding *et al.*, Phys. Rev. D 8, 3721 (1973). We are indebted to M. J. Tannenbaum for sending us the data before publication.

[39]F. W. Brasse *et al.*, Nucl. Phys. B39, 421 (1972).

[40]H. Fraas and D. Schildknecht, Nucl. Phys. B14, 543 (1969).

[41]This effect was first noted in the experiments reported in Refs. 15 and 19. There were, however, not enough events in those experiments to make a meaningful separation of ρ^0 and ω from nonresonant background. The quoted slopes refer to all events falling within a missing-mass interval around the ρ peak. Consequently, the t dependence of the background and of the ex-

perimental mass resolution had a serious effect on the slope measurements.
[42]See Moffeit, Ref. 36.
[43]See Ballam *et al.*, Ref. 36.
[44]B. L. Ioffe, Zh. Eksp. Teor. Fiz. Pis'ma Red. 9, 163 (1969) [JETP Lett. 9, 97 (1969)]; Phys. Lett. 30B, 123 (1969); H. T. Nieh, *ibid.* 38B, 100 (1972).
[45]H. Cheng and T. T. Wu, Phys. Rev. 183, 1324 (1969); R. W. Griffith, *ibid.* 188, 2112 (1969); H. D. I. Abarbanel and J. B. Kogut, Phys. Rev. D 5, 2050; P. Roy Phys. Lett. 41B, 325 (1972); G. Kramer and H. R. Quinn, Nucl. Phys. B55, 222 (1973); Pham Xuan Yem, Phys. Lett. 41B, 67 (1972).
[46]H. Meyer, in Proceedings of the International Symposium on Electron and Photon Interactions at High Energies, Bonn, 1973 (unpublished).
[47]J. M. Bailey *et al.*, report contributed to the International Symposium on Electron and Photon Interactions at High Energies, Bonn, 1973 (unpublished).
[48]See, for example, J. T. Dakin and G. Feldman, Phys. Rev. D 8, 2862 (1973).

PHYSICAL REVIEW D VOLUME 9, NUMBER 7 1 APRIL 1974

Study of the reaction $p+d\rightarrow He^3+x^0$

H. Brody,* E. Groves,*† R. Van Berg,* and W. D. Wales*
University of Pennsylvania, Philadelphia, Pennsylvania 19174

B. Maglich,‡ J. Norem,‡§ J. Oostens,‡‖ and M. Silverman¶
Rutgers, The State University, New Brunswick, New Jersey 08903

G. B. Cvijanovich
Upsala College, East Orange, New Jersey 07019
(Received 14 August 1973; revised manuscript received 28 December 1973)

The missing-mass technique has been used to study the spectra of neutral mesons produced by 2- and 3-GeV protons in the reaction $p+d\rightarrow He^3+x^0$. Cross sections $(d\sigma/d\Omega_{c.m.})$ of about 10^{-34} cm^2/sr were observed for the π, η, and ω for 3-GeV protons. A peak with a much smaller cross section was observed at a mass of 956 MeV. We have tentatively identified this peak as the η'. Cross sections for the π and η were nearly a factor of 10 larger at 2 GeV than at 3 GeV. Deviations from simple phase space were observed near the two-pion threshold in both 2-GeV and 3-GeV data. Details of the experimental method and of the results are presented.

I. INTRODUCTION

The constraints imposed by the kinematics of two-body interactions facilitate a very attractive experimental method of searching systematically for unstable particles or resonances. The CERN missing-mass spectrometer[1] has demonstrated the great power of a system designed to exploit these constraints. However, the CERN system and its successor, the boson spectrometer,[2] are limited to charged meson states, since they rely on the detection of the proton in the interaction $\pi^-+p\rightarrow p+x^-$. Three of the five well-established nonstrange mesons in the mass range below 1000 MeV (see Table I)[3] have isotopic spin zero and thus cannot be detected by a system similar to the boson spectrometer. In addition there are many other states under 1000 MeV which have been reported but whose existence has not been reliably established. A systematic search for neutral mesons in this mass region is thus easily justified. Although attempts have been made to extend the missing-mass technique to neutral mesons by using the reaction $\pi^-+p\rightarrow n+x^0$, the inherent difficulty in measuring the parameters of the neutron has limited both the resolution and the accuracy of the systematic searches which have been made.

The reaction $p+d\rightarrow He^3+x^0$ is the simplest accessible reaction which permits precise measurement of the parameters of all three of the known particles in a systematic search for neutral mesons. The experiment was envisioned as the first of a series of endeavors to exploit this reaction and ones similar to it, such as $p+d\rightarrow H^3+x^+$ (for isotopic-spin-1 particles) and $d+d\rightarrow He^4+x^0$ (for pure isotopic-spin-0 production). The termination of funding of the Pennsylvania-Princeton Accelerator (PPA) made such investigations impossible.

II. EXPERIMENTAL METHOD

Figure 1 shows the kinematics of the reaction for various mass values of neutral mesons pro-